The effect of the laser beam intensity profile in laser-based directed energy deposition A high-fidelity thermal-fluid modeling approach

Sattari, Mohammad; Ebrahimi, Amin; Luckabauer, Martin; Römer, Gert willem R.B.E.

DOI
10.1016/j.addma.2024.104227

Publication date
2024

Document Version
Final published version

Published in
Additive Manufacturing

Additive Manufacturing 86 (2024) 104227

Contents lists available at ScienceDirect

Additive Manufacturing

journal homepage: www.elsevier.com/locate/addma

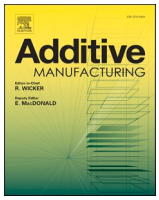

The effect of the laser beam intensity profile in laser-based directed energy deposition: A high-fidelity thermal-fluid modeling approach

Mohammad Sattari [a,*], Amin Ebrahimi [b], Martin Luckabauer [a], Gert-willem R.B.E. Römer [a]

[a] Department of Mechanics of Solids, Surfaces and Systems (MS3), Faculty of Engineering Technology, University of Twente, Drienerlolaan 5, 7522NB Enschede, The Netherlands
[b] Department of Materials Science and Engineering, Faculty of Mechanical Engineering, Delft University of Technology, Mekelweg 2, 2628CD Delft, The Netherlands

ARTICLE INFO

Keywords:
Metal additive manufacturing
High-fidelity thermal-fluid modeling
Computational fluid dynamics
Laser beam shaping
Laser energy attenuation

ABSTRACT

Modeling the thermal and fluid flow fields in laser-based directed energy deposition (DED-LB) is crucial for understanding process behavior and ensuring part quality. However, existing models often fail to accurately predict these fields due to simplifying assumptions, particularly regarding powder particle-induced attenuation in laser power and energy density distribution, and the variable material properties and process parameters. The present work introduces a high-fidelity multi-phase thermal-fluid model driven by a combination of the discrete element method (DEM) and the finite volume method (FVM). Incorporating an enhanced attenuation model for laser energy enables a more precise approximation of powder particle-induced attenuation effects in the laser power and energy density distribution. The study focuses on the influence of laser beam intensity profiles during DED-LB of austenitic stainless steel (AISI 316 L), with model validation conducted through experimental measurements of deposited track dimensions for different beam shapes. The results of numerical simulations demonstrate the critical impact of powder-induced attenuation on the laser power and intensity profiles. Neglecting laser energy attenuation, a common assumption in numerical simulations of DED-LB, leads to overestimations of the absorbed energy of the laser beam, affecting thermal and fluid flow fields, and melt pool dimensions. The present study unravels the complex relationship between the attenuation coefficient (due to the powder stream) and powder stream characteristics, describing the variations of the attenuation coefficient with changes in the powder mass flow rate and powder stream incidence angle. The findings show the critical effects of laser beam shaping on melt pool behavior in DED-LB, with square beams inducing larger melt pool volumes and circular beams creating smaller but deeper melt pools. The proposed enhanced thermal-fluid modeling framework offers a robust approach for optimizing laser-based additive manufacturing across diverse materials and laser systems.

1. Introduction

Laser-based directed energy deposition (DED-LB) is an additive manufacturing (AM) technique that enables the fabrication of complex three-dimensional structures with functional properties and relatively high precision [1]. DED-LB employs a laser beam to melt a powder feedstock material transported by a carrier gas and injected into a melt pool induced by a laser. The molten material is deposited in a controlled manner onto the substrate, where it solidifies into the desired form. The quality and microstructural properties of the parts manufactured using DED-LB critically depend on the successive laser-induced thermal cycles experienced by the material during production [2]. These thermal cycles are influenced by several factors, including the interaction between the powder stream and laser beam, the thermophysical properties of the material, and the geometry of the component [1,2]. Therefore, regulating the localized heating and cooling cycles presents the potential to manipulate the properties of additively manufactured parts.

The modulation of a laser beam's intensity profile, commonly referred to as laser beam shaping [3], allows to alter the dimensions of the melt pool [3,4], thereby influencing the thermal history, solidification behavior [5], and resulting microstructure of the deposited material [6]. For example, experimental investigations conducted by Partes and Sepold [7] demonstrated an extension of the DED-LB processing window through temporal modulation of the energy density of an Nd:YAG laser. Higginson et al. [8,9] employed holographic optical elements (HOEs) in

* Corresponding author.
E-mail addresses: m.sattari@utwente.nl (M. Sattari), A.ebrahimi@tudelft.nl (A. Ebrahimi), m.luckabauer@utwente.nl (M. Luckabauer), g.r.b.e.romer@utwente.nl (G.-w.R.B.E. Römer).

https://doi.org/10.1016/j.addma.2024.104227
Received 3 October 2023; Received in revised form 14 May 2024; Accepted 22 May 2024
Available online 23 May 2024

Nomenclature

α	absorption coefficient of laser energy [-]
α_{atten}	laser energy attenuation coefficient [-]
α_v	evaporation rate (accommodation) coefficient [-]
β_p	particle shape factor [-]
Γ	surface excess at saturation [mole·m^{-2}]
γ	surface tension coefficient [N·m^{-1}]
γ_m^0	surface tension coefficient of pure metal at melting temperature [N·m^{-1}]
$\left(\frac{\partial\gamma}{\partial T}\right)^0$	temperature gradient of the surface tension coefficient of the pure molten metal [N·m^{-1}·K^{-1}]
γ_v	ratio of specific heats for the vapor [-]
ε_s	emissivity of the metal surface [-]
θ	incidence angle of the laser beam with respect to normal on surface [°]
θ_p	incidence angle of the powder particle relative to the horizontal (surface) [°]
θ_p'	angle of reflection of the powder particle relative to the horizontal (surface) [°]
κ	surface curvature [radm^{-1}]
λ_1	primary dendrite arm spacing [m]
μ	dynamic viscosity [Pa·s]
ρ	material density [kg·m^{-3}]
ρ_g	shielding gas density [kg·m^{-3}]
ρ_p	particle material density [kg·m^{-3}]
σ	Stefan-Boltzmann constant [W·m^{-2}·K^{-4}]
A_p	powder particle surface area [m^2]
a	thermodynamic activity of surface-active element [mole·m^{-3}]
$\vec{b}_{sol}$	momentum source for solidification flow losses [m·s^{-2}]
$\vec{b}_{src}$	momentum source term corresponding to drag against particles entering the melt pool [m·s^{-2}]
C_0	weight percentage of alloy elements [wt%]
c_{atten}	attenuation model constant [-]
$C_{D,p}$	particle drag coefficient [-]
$C_{D,s}$	solidification drag coefficient [-]
c_p	pressure-specific heat capacity [J·kg^{-1}·K^{-1}]
c_v^{vap}	volume-specific heat capacity of vapor [J·kg^{-1}·K^{-1}]
d_p	diameter of a spherical powder particle [m]
d_{str}	apparent powder stream diameter [m]
e_i^j	activity interaction coefficient between elements i and j [-]
e_p	coefficient of restitution [-]
F	volume fraction of fluid [-]
EDF	energy density factor [-]
EDF_{atten}	attenuated energy density factor [-]
f_s	solid fraction [-]
$\vec{f}_{surf}$	momentum source for gas-metal interface forces [m·s^{-2}]
$\vec{g}$	gravitational acceleration [m·s^{-2}]
h	specific enthalpy of metal [J·kg^{-1}]
h_w	heat transfer coefficient [W·m^{-2}·K^{-1}]
I_L	spatial laser beam intensity profile [W·m^{-2}]
k	thermal conductivity [W·m^{-1}·K^{-1}]
k_a	element activity coefficient [-]
L_α	standard heat of adsorption [J·mole^{-1}]
L_c	characteristic length of the melt pool [m]
L_f	latent heat of fusion [J·kg^{-1}]
L_L	laser beam cylinder length [m]
L_{str}	powder stream cylinder length [m]
L_v	latent heat of vaporization [J·kg^{-1}]
m_p	powder particle mass [kg]
$\dot{m}_{src}$	powder mass addition [kg·s^{-1}]
Ma	Marangoni number [-]
N_{ae}	number of the surface-active elements [-]
N_d	number of particle diameter discretization levels
N_e	number of alloy elements
N_{iter}	number of numerical iterations to establish laser energy attenuation
N_{lp}	number of points in energy density distribution
N_p	total number of particles
N_{shaded}	number of occurrences a laser energy density point is shaded
$\vec{n}$	surface unit normal vector
n_p	number of particles with diameter d_p
P	pressure [Pa]
P_0	initial (atmospheric) pressure [Pa]
Pe	Peclet number [-]
PND	particle number density [%]
PSD	particle size distribution [%]
P_v	vapor saturation pressure [Pa]
Q_{surf}	energy absorption and loss source term [W·m^{-3}]
R	ideal gas constant [J·mole^{-1}·K^{-1}]
Re	Reynolds number [-]
$\vec{R}_L$	laser beam ray vector
$\vec{R}_{L,ref}$	reflected laser beam ray vector
r_L	radius of laser beam [m]
r_{str}	apparent radius of powder particle stream [m]
S	entropy factor for segregation [-]
T	temperature [K]
T_0	initial temperature [K]
T_l	liquidus temperature [K]
T_m	melting temperature [K]
T_{peak}	peak temperature in the melt pool [K]
T_s	solidus temperature [K]
T_v	vapor saturation (boiling) temperature [K]
t	time [s]
t_{pg}	particle generation time [s]
V_p	particle volume [m^{-3}]
$\vec{V}_D$	Darcy's microscopic inter-dendritic fluid velocity [m·s^{-1}]
$\vec{v}$	velocity vector [m·s^{-1}]
$\vec{v}_g$	shielding gas velocity vector [m·s^{-1}]
v_{peak}	peak fluid velocity in the melt pool [m·s^{-1}]
$\vec{v}_p$	powder particle velocity vector [m·s^{-1}]
$\vec{x}_p$	Position vector of the powder particle [m]

conjunction with a CO_2 laser source to control the laser beam intensity profile in DED-LB. Their findings revealed that the melt pool shape and the resulting microstructure of the deposits could be tailored through laser beam shaping. Shang et al. [10] further demonstrated the control of microstructure homogeneity and grain size in DED-LB by modulating the intensity profile of a circular laser spot. Similar observations have been corroborated in experiments utilizing various beam shapes, including top-hat, annular (ring), square-shaped, and so-called "rugby posts" shapes [11–15]. These experimental investigations collectively demonstrate the significant potential of laser beam shaping in controlling localized heating and cooling cycles during laser-based metal additive manufacturing. However, most of the existing literature on

DED-LB utilizes Gaussian laser intensity profiles, while the effects of modulating the laser beam intensity profile on the process behavior and the resulting properties and microstructure of the fabricated parts are not well understood.

Computational modeling is a powerful tool for studying the thermal and fluid flow fields in DED-LB and optimizing the process parameters to achieve desired part quality and properties. However, assumptions made to develop computationally efficient models often lead to limitations that hinder the predictive capability and applicability of the models [16]. One of the major limitations in computational models developed for DED-LB is the neglect of the complex interactions of the laser beam and the stream of flying powder particles. These complex interactions can result in significant energy attenuation of the laser beam due to scattering and absorption by the powder particles, leading to a reduction of the laser power available for melting the substrate material [17]. Moreover, these interactions can alter the spatial intensity distribution of the laser beam, leading to a deviation from the original intensity profile reaching the substrate [18]. Conversely, temporal and spatial changes in the thermal profiles due to variations in the laser beam intensity profile can affect the laser energy absorption and the shape of the resulting melt pool [4,19]. The effects of these interactions on the heat and fluid flow behavior in DED-LB are not well understood and are often addressed by introducing empirical calibration factors or tuning parameters into the models. For example, many models employ a parameter referred to as "catchment efficiency" to account for the fraction of powder particles entering the molten pool and contributing to the deposition process [20–24]. The catchment efficiency is subject to several parameters, including the laser beam shape, the powder mass flow rate, and the position and angle of the laser beam relative to the powder stream [25]. Therefore, it is necessary to calibrate the value of the catchment efficiency for each set of processing parameters based on experimental measurements to obtain accurate numerical predictions, which demands considerable time and computational expenses.

The dimensions and shape of the laser beam intensity profile are important factors influencing the thermal and fluid flow fields in DED-LB. As is the case in experimental studies, as mentioned above, most of the existing computational models for DED-LB use circular laser beams with Gaussian or uniform intensity profiles. However, the latter may not be suitable for all processing conditions and may lead to some challenges in DED-LB, such as overheating, underheating, instability, and asymmetry of the melt pool and undesirable microstructure, as the energy concentrates at the core of the Gaussian laser beam profile. Thus, DED-LB favors more uniform intensity distributions [26–28], as they result in more even temperature distribution. Chen et al. [23] presented a thermal-fluid numerical simulation driven by the finite element method to describe the relationship between the microstructure characteristics and the thermal profiles in co-axial powder-fed laser cladding. They assumed a circular laser beam exhibiting a Gaussian intensity profile and ignored the attenuation of the laser power caused by the scattering and absorption of light by the powder particles. Zhang et al. [29] presented a computational model based on the finite volume method to examine the effects of laser power and scanning speed, sulfur content in stainless steel, and powder mass flow rate on the clad geometry in DED-LB. They adopted a circular laser beam with a uniform intensity profile and excluded the laser beam's interaction with the powder stream. Wu et al. [20] proposed a simulation framework to study the complete-phase heat transfer and mass transport in co-axial DED-LB. They used a circular laser beam displaying a Gaussian intensity profile and estimated the energy attenuation according to the Lambert-Beer law. Gao et al. [30] applied a three-dimensional computational model to investigate transient thermal and fluid flow fields in the DED-LB of an Invar alloy. Their model employed a circular laser beam having a Gaussian intensity profile. These studies enhance the understanding of thermal and fluid flow fields in DED-LB with circular laser beams. However, they have some limitations as they do not account for the effects of surface temperature and laser beam incidence angle on the absorption of laser energy by the substrate material, which can vary significantly during DED-LB. Therefore, a comprehensive yet computationally efficient model for considering all influencing parameters and phenomena in the DED-LB process is still lacking. Additionally, more research is needed to analyze the effects of laser beam shaping on heat transfer and fluid flow behavior in DED-LB.

The present work overcomes the above-mentioned limitations of existing models in literature by developing an advanced high-fidelity multi-phase thermal-fluid model that does not suffer from these limitations. In addition, this model is employed to study the effects of laser beam shaping on heat transfer and mass transport in DED-LB of AISI 316 L austenitic stainless steel, a frequently used material in metal additive manufacturing. As previously noted, uniform laser intensity profiles are usually favorable in DED-LB. The model is employed to simulate three different laser beam shapes (circular, ring, and square), all with uniform intensity profiles. These three beam shapes, being the most commonly utilized, serve to demonstrate and validate the capability of the present thermal-fluid model to predict the effects of laser beam shaping and to offer a comparative analysis of the influence of these beam shapes in DED-LB. The dynamics of powder particles during DED-LB are explicitly incorporated into the model. A novel energy attenuation model is proposed that accounts for the complex interaction of the laser beam with the stream of powder particles. To validate the model predictions, experimental measurements are performed to determine the dimensions of deposited tracks for different beam shapes. Also, the uniqueness of the present model lies in the proper incorporation of influencing physical phenomena and parameters without the need for specific model calibration to accommodate particular laser beam intensity profiles. Despite the primary focus of this work on laser beam shaping, this model can be employed to study the impact of other process parameters, such as the laser power, scanning velocity, powder mass flow rate, and powder particle size. This study enhances our understanding of heat transfer and fluid flow behavior in DED-LB and offers a valuable tool for investigating process stability, optimizing process parameters, and improving part quality and performance.

2. Model description

The evolution of heat and fluid flow in DED-LB, as shown schematically in Fig. 1, is numerically studied in the present work. In the present DED-LB process, a laser beam, incident perpendicularly to the substrate's surface, is employed as a source to heat the substrate's surface and powder particles. Powder particles exit the powder nozzle and are transported towards the surface by an inert carrier gas (typically argon). The experimental setup and procedure are described in detail in Section ↱4. The interaction of the laser beam with the powder particles and the substrate heats up the particles and substrate, leading to fusion and the creation of a molten pool. Following the synchronized movement of the laser beam and the powder nozzle at an identical velocity, the melt pool undergoes solidification, forming a deposition track on the substrate, commonly referred to as a bead. Through an additional nozzle, an inert gas is employed as the shielding gas to prevent oxidation of the molten metal. An austenitic stainless steel alloy (AISI 316 L), with the composition listed in Table 1, is used for both the substrate and powder. In Table 2 and Fig. 2, the thermophysical properties of AISI 316 L used in the numerical simulations are presented.

In the present study, a three-dimensional multi-phase thermal-fluid model is developed based on the finite volume method [35] to study the transient thermal and fluid flow fields in DED-LB. The liquid metal is assumed incompressible and modeled as a Newtonian fluid. Moreover, it is assumed that the molten metal flow is laminar. Accordingly, mass, momentum, and energy conservation are governed by the equations defined as follows, respectively [21,36]

$$\nabla \cdot \vec{v} = 0, \tag{1}$$

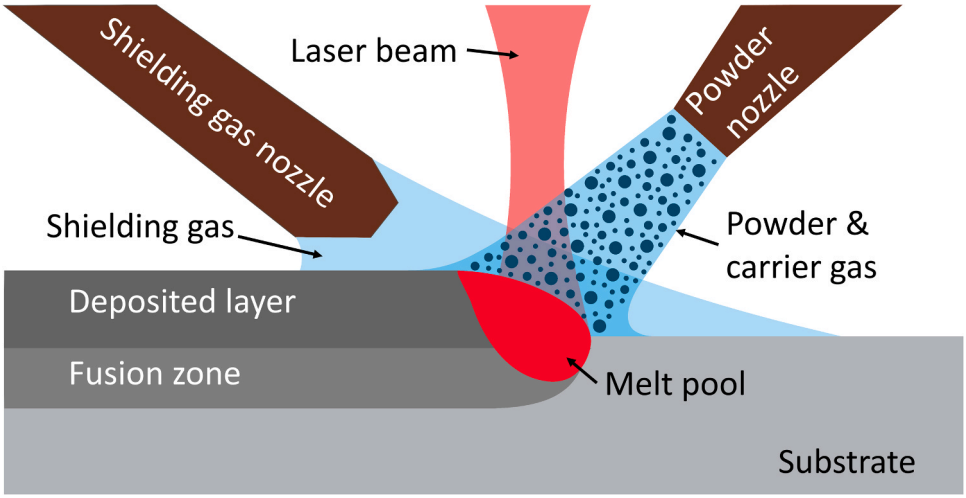

Fig. 1. Schematic representation of laser-based directed energy deposition (DED-LB).

Table 1
Composition of AISI 316 L. The data were taken from the Oerlikon Metco product data sheet [31].

Element i	Fe	Cr	Mo	Ni	Si	C	S
C_{0i} [wt%]	66.14	17	2.5	12	2.3	0.03	0.03

Table 2
Constant thermophysical properties of AISI 316 L used in the present study.

Property	Value	Unit
Solidus temperature T_s [32]	1637	K
Liquidus temperature T_l [32]	1715	K
Latent heat of fusion L_f [33]	$2.6{\cdot}10^5$	J·kg^{-1}
Vapor saturation pressure P_v [34]	$1.013{\cdot}10^5$	Pa
Vapor saturation (boiling) temperature T_v [34]	3134	K
Latent heat of vaporization L_v [34]	$6.08{\cdot}10^6$	J·kg^{-1}
Ratio of specific heats for the vapor γ_v [34]	1.67	-
Volume-specific heat capacity of the vapor c_v^{vap} [34]	449	J·kg^{-1}·K^{-1}

$$\rho\left(\frac{\partial \vec{v}}{\partial t}+\vec{v}\cdot\nabla\vec{v}\right)=-\nabla P+\nabla\cdot\left\{\mu\left[\nabla\vec{v}+(\nabla\vec{v})^T\right]\right\}+\rho\left(\vec{g}+\vec{b}_{sol}+\vec{f}_{surf}\right), \tag{2}$$

$$\rho\left[\frac{\partial h}{\partial t}+\nabla\cdot(h\vec{v})\right]=\nabla\cdot(k\nabla T)+Q_{surf}. \tag{3}$$

The enthalpy-porosity method [37] is employed to model solidification and melting. Accordingly, the total enthalpy of the material (h) is defined as the sum of the latent heat and the sensible heat and is modeled as [37]

$$h(T)=\begin{cases}\int_{T_0}^{T}c_p dT, & T\le T_s\\ h(T_s)+(1-f_s)L_f, & T_s<T\le T_l\\ h(T_l)+\int_{T_l}^{T}c_p dT, & T_l<T\end{cases}. \tag{4}$$

A sink is introduced into the momentum equation to model the damping of molten metal velocity in the mushy region, as well as the suppression of molten metal velocities in the solid regions [34,36,38,39]. The sink term is defined as

$$\vec{b}_{sol}=-C_{D,s}\frac{f_s^2}{(1-f_s)^3}\vec{V}_D, \tag{5}$$

where, $C_{D,s}$ is the solidification drag coefficient, and its value can be approximated using the following expression.

$$C_{D,s}=\frac{180\mu}{\lambda_1^2\rho}, \tag{6}$$

where μ is the dynamic viscosity of the material, λ_1 is the average primary dendritic arm spacing, and ρ is the density of the material. As reported by Ma et al. [40], the average primary dendritic arm spacing, λ_1, is approximately 3 μm in laser cladding of AISI 316 L, using a similar range of laser power and travel velocity as considered in this study. Utilizing the viscosity (μ) and density (ρ) values at the melting temperature of the material, the solidification drag coefficient, $C_{D,s}$, can be approximated as $2.2{\cdot}10^7$ s^{-1}. This approximation agrees with the criterion outlined by Ebrahimi et al. [41].

The Volume of Fluid (VOF) method [42] is used to track the gas-metal interface of the melt pool. In the VOF method, the volume fraction of the metal phase in a computational cell is represented by a scalar variable, F, ranging between 0 and 1. A value of $F=1$ reflects that the cell is fully occupied by the metal phase, while a value of $F=0$ indicates that the cell is entirely in the gas region. Computational cells with $0<F<1$ are located at the gas-metal interface. These cells represent the regions where metal and gas phases coexist, with F indicating the relative volume of the metal phase present within the cell compared to the total cell volume. The variation in the scalar function F is governed by the linear advection equation, which is defined as

$$\frac{\partial F}{\partial t}+\nabla\cdot(F\vec{v})=0. \tag{7}$$

To take into account the influences exerted on the interface between gas and metal, a momentum source term, $\vec{f}_{surf}$, is defined based on a continuous surface force model [43] as Eq. (8), where capillary force, Marangoni shear force, recoil pressure, and carrier-shielding gas pressure are the terms on the right-hand side of the equation below,

$$\vec{f}_{surf}=\left\{\gamma\kappa\vec{n}+\frac{d\gamma}{dT}[\nabla T-\vec{n}(\vec{n}.\nabla T)]+\alpha_v P_v\exp\left[\frac{L_v}{c_v^{vap}(\gamma_v-1)}\left(\frac{1}{T_v}-\frac{1}{T}\right)\right]\vec{n}+\frac{\rho_g}{2}(\vec{n}.\vec{v_g})^2\right\}\|\nabla F\|\frac{2}{\rho_m+\rho_g}, \tag{8}$$

where m and g represent metal and gas, respectively. $\vec{n}=\nabla F/\|\nabla F\|$ is

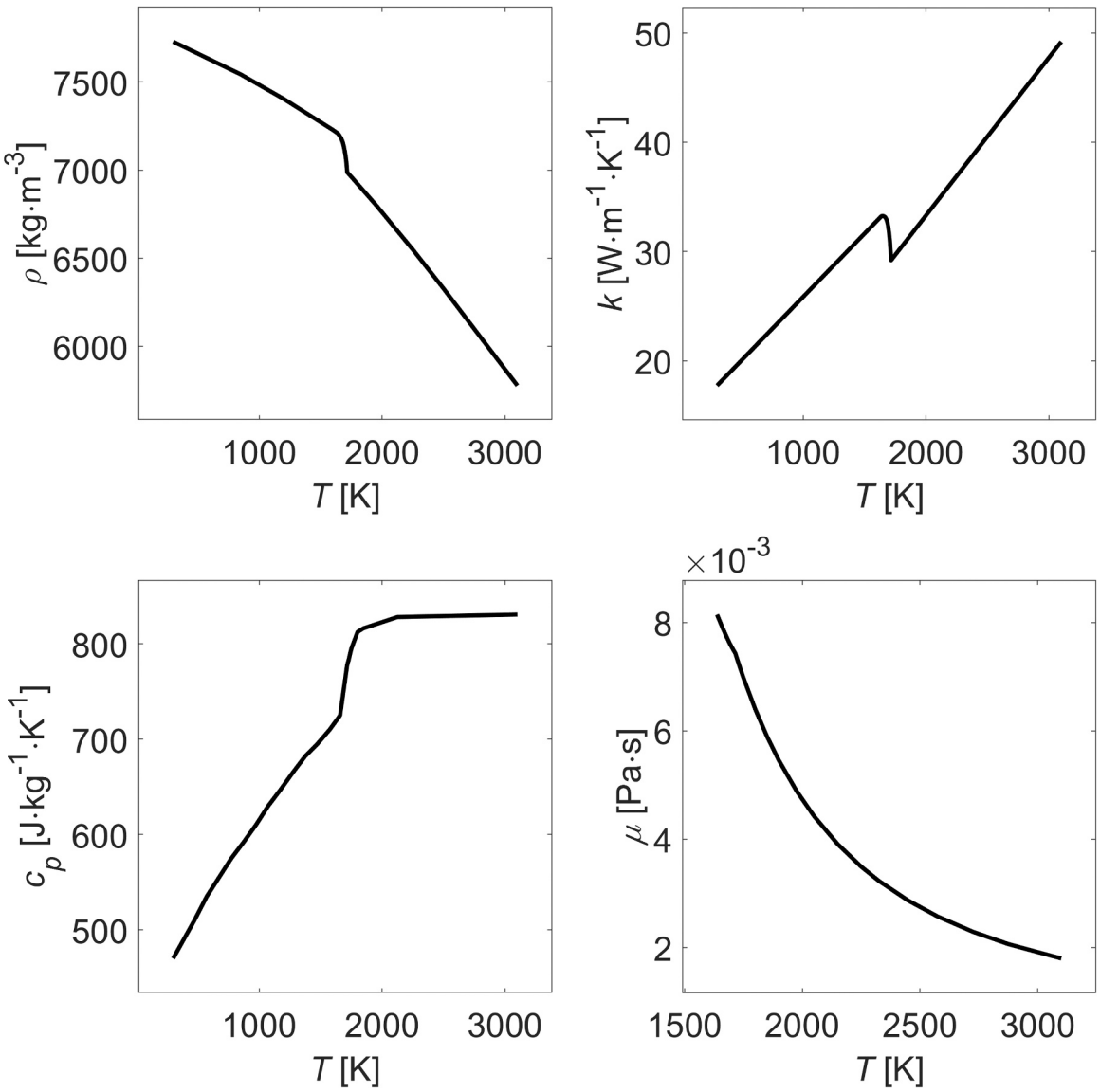

Fig. 2. Temperature-dependent thermophysical properties of AISI 316 L. The data were obtained using the software tool JMatPro CALPHAD [32].

the unit vector normal to the surface, $\kappa = \nabla.\vec{n}$ is the curvature of the surface [19]. The third term on the right-hand side of the equation above represents the recoil pressure on the surface of the melt pool due to the metal evaporation and is calculated using the Clapeyron equation [44]. The Stokes number represents the ratio of particle response time to flow field time scale [45]. In the present study, this number is larger than the unity for the particles in relation to the shielding or carrier gas flow, signifying that the velocity of the powders is dominated by inertia and is hardly affected by the carrier and shielding gases; thus, the influence of shielding and carrier gas flow on the velocity and trajectory of powder particles can be reasonably neglected. Furthermore, according to Ebrahimi et al. [4,5,19,90], the combined influence of radiation and heat convection by the shielding gas on heat loss from the substrate surface is negligible, constituting only about 0.3% of the absorbed laser power. Therefore, the shielding gas flow is not incorporated into the present model. However, the dynamic pressure of the carrier-shielding gas applied on the free surface of the melt pool is taken into account by the last term on the right-hand side of the equation above, where $\vec{v_g}$ is the gas velocity vector [34].

The surface tension of molten steel alloys is significantly influenced by surface-active elements [46]. The surface tension model employed in the present work accounts for the influence of surface-active elements, including oxygen and sulfur, on the surface tension coefficient of molten steel alloys. The model also incorporates the effect of temperature on the variation of the surface tension coefficient. Accordingly, the value of the surface tension coefficient, γ, can be approximated as follows [47,48],

$$\gamma = \gamma_m^0 + \left(\frac{\partial\gamma}{\partial T}\right)^0 (T - T_m) - \sum_i^{N_{ae}} \left[RT\Gamma_i \ln\left(1 + S_i a_i e^{-\frac{L_{ai}}{RT}}\right)\right]. \quad (9)$$

Here, a_i is the thermodynamic activity of the surfactants defined as

$$a_i = k_{ai}\cdot[\text{wt\%}i], \quad (10)$$

where, k_{ai} is the activity coefficient of element i (referring to sulfur and oxygen). The value of k_{ai} is determined as

$$\log k_{ai} = \sum_j^{N_e} e_i^j \cdot [wt\%j], \quad (11)$$

where, e_i^j is the activity interaction coefficient between elements i and j. Table 3 presents the values used in the above surface tension model. Table 4 lists the activity interaction coefficients (e_i^j) for AISI 316 L. The AISI 316 L surface tension coefficient change with

Table 3
Parameters in the AISI 316 L austenitic stainless steel surface tension model.

Parameter	Value	Unit
Surface tension coefficient of pure metal at melting temperature γ_m^0 [47]	1.943	$N{\cdot}m^{-1}$
Temperature gradient of the surface tension coefficient of the pure molten metal $\left(\frac{\partial\gamma}{\partial T}\right)^0$ [49]	-4.3·10^{-4}	$N{\cdot}m^{-1}{\cdot}K^{-1}$
Segregation entropy factor for sulfur S_S [47]	3.18·10^{-3}	-
Segregation entropy factor for oxygen S_O [47]	13.8·10^{-3}	-
Surface excess at saturation for sulfur Γ_S [47]	1.3·10^{-5}	$mole{\cdot}m^{-2}$
Surface excess at saturation for oxygen Γ_O [47]	2.03·10^{-5}	$mole{\cdot}m^{-2}$
Standard heat of adsorption for sulfur $L_{\alpha S}$ [50]	-1.662·10^5	$J{\cdot}mole^{-1}$
Standard heat of adsorption for oxygen $L_{\alpha O}$ [47]	-1.463·10^5	$J{\cdot}mole^{-1}$

Table 4
Element activity interaction coefficients of AISI 316 L, following from Eq. (9) and Table 3.

Element j	e_O^j	e_S^j
Cr	-0.046 [51]	-94.2/T+0.0396 [52]
Mo	0 [51]	0 [53]
Ni	0.006 [47]	0.003 [53]
Si	-0.066 [51]	0.063 [47]
C	-0.42 [53]	0.11 [47]
S	-0.133 [47,51]	-0.028 [47]
O	-1750/T+0.76 [51]	-0.27 [47]

temperature, shown in Fig. 3, is approximated using Eq. (9).

The energy of the laser beam absorbed by the material and heat loss due to convection, radiation, and vaporization are modeled by incorporating a heat source term (Q_{surf}) into the energy equation (Eq. 3) [19,54],

$$Q_{surf} = \left\{ \alpha(T,\theta) I_L - h_w(T - T_0) - \varepsilon_s \sigma\left(T^4 - {T_0}^4\right) - \frac{\alpha_v P_v}{\sqrt{2\pi c_v^{vap}(\gamma_v - 1)T}} \exp\left[\frac{L_v}{c_v^{vap}(\gamma_v - 1)}\left(\frac{1}{T_v} - \frac{1}{T}\right)\right] \right\} \|\nabla F\| \frac{2\rho c_p}{(\rho c_p)_m + (\rho c_p)_g}. \tag{12}$$

The absorptivity is approximated using an enhanced absorptivity model introduced in our previous work [19], which accounts for surface temperature, material composition, laser wavelength, and laser beam incidence angle. Furthermore, multiple reflections and absorptions of the laser rays in the laser beam, when interacting with the substrate and deposited layer, are modeled using a ray tracing technique [55]. A ray is

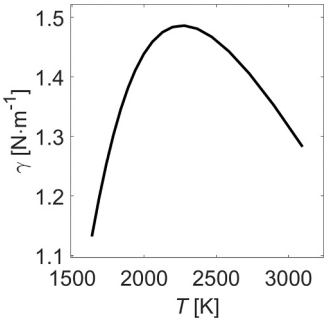

Fig. 3. Calculated surface tension coefficient, γ, of AISI 316 L austenitic stainless steel as a function of temperature.

defined as a part of the laser beam irradiating a grid cell. The laser energy is absorbed by the base material at the irradiation point, with the rest reflecting as a new beam. The direction of the reflected ray, $\vec{R}_{L,ref}$, is calculated using,

$$\vec{R}_{L,ref} = \vec{R}_L - 2\left(\vec{R}_L \cdot \vec{n}\right)\vec{n}, \tag{13}$$

where $\vec{R}_L$ is the laser beam ray vector before the reflection. Ray tracking stops when 99% of the initial ray energy is absorbed [55].

The position and velocity of powder particles are modeled by employing the discrete element method (DEM) [56]. The position and velocity of powder particles follow Newton's second law, which can be expressed as [36]

$$\frac{\partial(\vec{x}_p)}{\partial t} = \vec{v}_p, \tag{14}$$

$$\frac{\partial \vec{v}_p}{\partial t} = -\frac{\nabla P}{\rho_p} + \vec{g} + \vec{b}_{src}, \tag{15}$$

where $\vec{x}_p$, $\vec{v}_p$ and ρ_p are the position and velocity vectors, as well as the density, of the powder particle. A particle-fluid interaction model is employed to model the drag force encountered by the particles entering the melt pool. The momentum source term defining this drag force can be calculated by including an empirically determined drag coefficient, $C_{D,p}$ [34,36],

$$\vec{b}_{src} = \frac{\rho}{\rho_p}\left[\frac{3}{4d_p}\beta_p C_{D,p}\left(\vec{v} - \vec{v}_p\right)\left|\vec{v} - \vec{v}_p\right| + \frac{1}{2}\left(\frac{d\vec{v}}{dt} - \frac{d\vec{v}_p}{dt}\right)\right], \tag{16}$$

where

$$C_{D,p} = \frac{24}{\mathrm{Re}} + \frac{6}{1 + \sqrt{\mathrm{Re}}} + 0.4, \tag{17}$$

and

$$\mathrm{Re} = \frac{\rho d_p \left|\vec{v} - \vec{v}_p\right|}{\mu}. \tag{18}$$

Here, β_p is the shape factor of the particles and represents the sphere-to-particle surface area ratio with equal volumes [34]. To determine the corresponding shape factor, a sample is taken randomly from the powder feedstock used in the experiments, as shown in Fig. 4. Each powder particle is fitted by an ellipse. The third ellipsoid diameter, perpendicular to the plane, as shown in Fig. 4, is assumed to be equal to the smaller diameter of the corresponding ellipse in the plane. Then, the shape factor of the corresponding ellipsoid is calculated. The average of these shape factors is found to be equal $\beta_p = 1.0588$.

According to the lumped-capacitance method, the temperature rise of a flying particle due to interaction with the laser beam can be expressed as [36]

$$m_p c_p(T)\frac{dT}{dt} = \alpha(T) I_L \frac{A_p}{4} - h_w A_p(\mathrm{T} - T_0) - \varepsilon_s \sigma A_p\left(T^4 - {T_0}^4\right). \tag{19}$$

The effective heat transfer coefficient between a powder particle and its host medium is calculated based on the particle velocity and Nusselt number correlations for solid spheres [57]. Due to the low powder mass flow rate and particle concentration in this study, it is assumed that

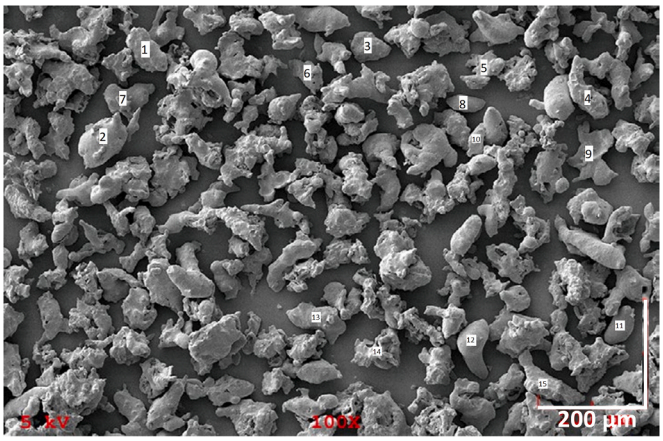

Fig. 4. SEM (scanning electrode microscope) micrograph of a random selection of powder particles (adopted from the Oerlikon Metco data sheet [31]) used in the experiments.

there are no interactions among particles, they do not displace fluid, and their influence on the liquid metal within the melt pool is negligible, as demonstrated in [58]. Moreover, particles are subject to heat transfer and phase change between solid, liquid and vapor [34,54]. The multiple bouncing of solid particles after the collision with the solid surface is neglected in this model. Nevertheless, their effect on laser energy is accounted for in the laser energy attenuation model. It is assumed that upon entry into the melt pool in a liquid state or subsequent melting within the melt pool, a particle is extracted from the calculation while its mass, momentum, and energy are incorporated into those of the continuous liquid metal.

Modeling the powder stream requires calculating the flow of powder particles as they emerge from the nozzle (Figs. 1 and 12b). Given the powder mass rate of 2.5 g·min^{-1} in this research study and the measured particle size distribution (see Section 4), the generation rate of particles, $\dot{n}_{p,i}$, with diameter $d_{p,i}$, as shown in Fig. 5 (vertical axis), can be calculated using

$$\dot{n}_{p,i} = \frac{\dot{m}_{src}}{\rho V_{p,i}} \frac{PSD_i}{100}. \tag{20}$$

The total particle generation rate, $\dot{N}_p$, then reads

$$\dot{N}_p = \sum_{i=1}^{N_d} \dot{n}_{p,i}. \tag{21}$$

As a result, the number density of particles, *PND*, as shown in Fig. 5 (right axis), can be calculated as

$$PND_i = \frac{\dot{n}_{p,i}}{\dot{N}_p} \cdot 100 = \frac{\frac{PSD_i}{V_{p,i}}}{\sum_{i=1}^{N_d} \frac{PSD_i}{V_{p,i}}} \cdot 100. \tag{22}$$

According to Pinkerton et al. [59,60], the stream of flying powder particles reaches its highest density with a Gaussian distribution at its cross-section. After this "focus," the powder flow diverges while maintaining its Gaussian distribution [25]. Therefore, in this study, the powder particle stream is modeled numerically to consist of horizontally distributed cubic particle sources with particle generation rates following a two-dimensional Gaussian distribution. The apparent radius of the powder stream, where the powder stream concentration drops to $1/e^2$ of its peak value at the center [22], is half the size of the actual radius. This apparent radius can be expressed as

$$r_{str} = \frac{d_{str}\sin(\theta_p)}{2}, \tag{23}$$

where d_{str} is the measured horizontally projected (apparent) diameter of the powder stream depicted in Fig. 12b, and θ_p is the powder stream incidence angle relative to the horizontal. To calculate the powder generation rate of cubic sources, a standard deviation of $d_{str}/4$ is considered. The powder sources and the calculated powder generation rate for these sources are illustrated in Fig. 6.

The interaction between the laser beam and the stream of powder particles substantially influences the quality of the deposited tracks, as indicated by prior research [22,61]. Analytical and numerical models were created to describe this interaction. Analytical models for off-axis [22,61–64] and co-axial [17,24,65–69] DED-LB, were built upon the classical Lambert-Beer law, which relates the attenuation of incident light to the properties of the material through which it traverses and Mie's theory, which describes how light scatters when interacting with particles. While analytical models are faster than numerical models, they exhibit certain constraints, such as ignoring particle rebound after collision with solid surfaces and the particle velocity distribution with respect to the powder stream radius. Numerical models [70–72] offer a higher accuracy compared to analytical models but are computationally demanding. Thus, incorporating numerical models into thermal-fluid models for DED-LB simulations is challenging.

The presence of a stream of powder particles in the laser beam can lead to a reduction in laser energy reaching the substrate. Furthermore, the powder stream may locally reduce the laser beam intensity due to "shadowing effect". Therefore, in the present work, a new laser energy attenuation model is presented to take into account the attenuation of both the power and the energy density of the laser beam caused by powder particles traveling through the laser beam, before and after bouncing from the underlying surface. It is important to note that this model operates independently of the DEM method. In this model, the effects of shielding and carrier gas flows on the velocity of powder particles are neglected. The effect of gravity is also neglected, because it does not affect the particle's horizontal position and velocity, when passing through the laser beam. It is also presumed that the substrate has a smooth surface, rendering the effect of friction on the horizontal component of the particle velocity neglectable. The collision of the

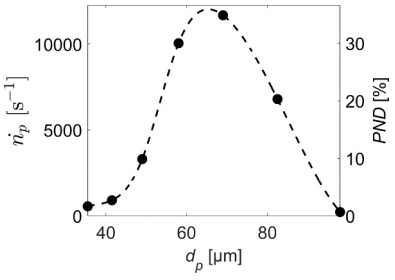

Fig. 5. Calculated powder particle generation rate, $\dot{n}_p$, on the left axis and powder particle number density (*PND*) on the right axis, for a 2.5 g·min^{-1} powder mass rate. The dashed curve is added as a visual aid.

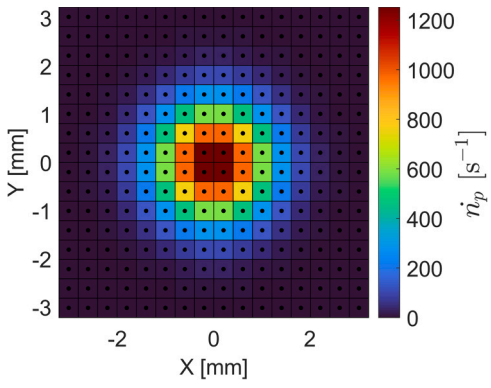

Fig. 6. Normal distribution of powder particle generation rates (0.75 mm standard deviation) at 2.5 g·min^{-1} mass rate.

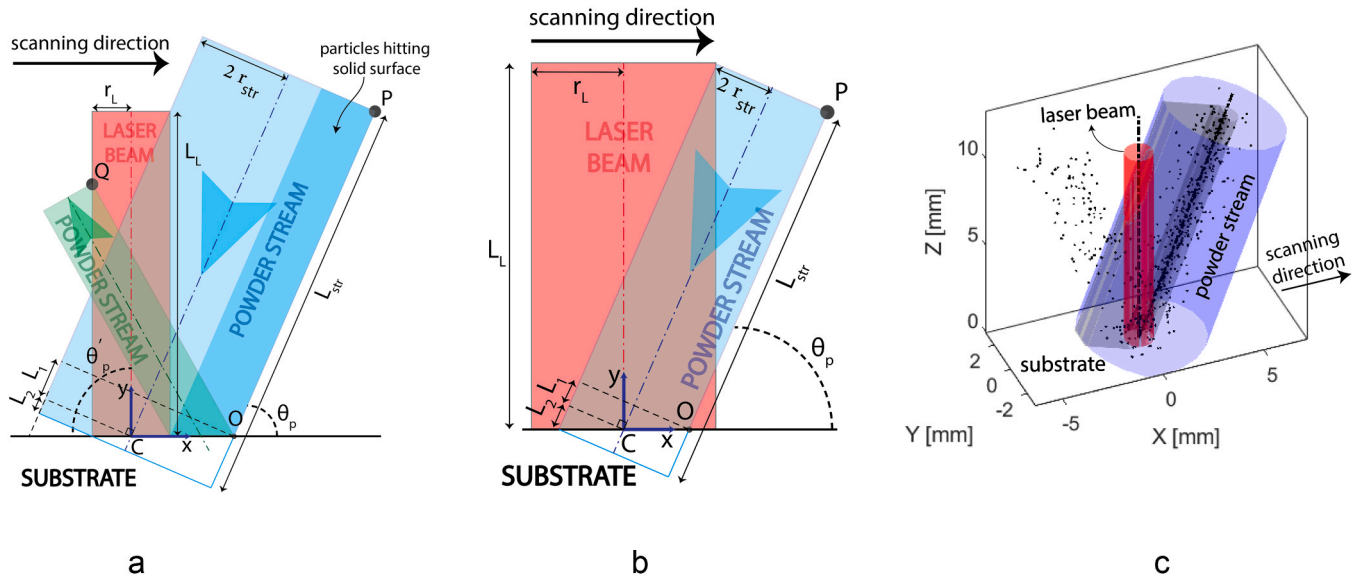

Fig. 7. Schematic of laser energy attenuation model. Two scenarios: (a) Wider powder stream than the laser beam on the substrate, (b) Smaller powder stream than the laser beam. (c) Laser cylinder (red), powder particles in the stream (blue), and particles bouncing off the surface.

flying particles with the underlying surface is posited to be partially elastic. Additionally, the assumption is made that the laser scanning speed remains moderate to prevent the formation of a melt pool with a width smaller than the diameter of the laser beam.

Fig. 7a and b show the two-dimensional schematic of two cases with different powder stream cylinder positions and sizes relative to the laser beam's position. Fig. 7c shows a three-dimensional representation of the laser and powder "cylinders". When $2r_{str}/\sin(\theta_p) \geq r_L$, the cylinder encasing the powder stream on the substrate has a larger diameter than the laser beam cylinder (Fig. 7a). In this case, powder particles that hit the surface in front of the laser beam (dark blue) enter the laser beam after bouncing from the surface. However, particles interacting with the laser beam prior to reaching the surface of the substrate either join the melt pool or hit the solidified surface of the substrate at the back of the laser beam, thereby eliminating any chance of reentering the beam. Conversely, when $2r_{str}/\sin(\theta_p) < r_L$, the powder flow cylinder positioned on the substrate possesses a smaller diameter than the laser beam cylinder (Fig. 7b). In this case, it is assumed that all the powder particles enter the melt pool without experiencing surface bounce. The radius of the laser cylinder, r_L, which is representative of the (arbitrary) laser beam intensity profile, is defined as the distance from the center C of the laser spot to the farthest away energy density point on the substrate (see Figs. 7a and b).

As illustrated in Fig. 7a, when $2r_{str}/\sin(\theta_p) \geq r_L$, a powder particle passing point P will reach point Q, after bouncing at point O and losing some kinetic energy, determined by the coefficient of restitution, e_p. This velocity restitution coefficient is the ratio of post-collision to pre-collision normal velocities for a particle hitting a solid surface, and is 0.88 for steel-steel impact [73]. The angle of reflection of powder particles, θ_p', is smaller than the angle of the incidence, θ_p, due to the loss of kinetic energy upon collision. To calculate the required lengths for the powder cylinder, L_{str}, and the laser beam cylinder, L_L, the farthest distance a particle must travel to pass the laser beam after bouncing from the surface, $\overline{OQ}$, is used. When assuming a partially elastic collision, $\overline{OP}\cos(\theta_p) = \overline{OQ}\cos(\theta_p')$. On the other hand, the vertical distance travelled by a particle, before and after the impact, follows $\overline{OP}\sin(\theta_p)e_p = \overline{OQ}\sin(\theta_p')$. Combining these two equations, the angle of the bouncing particle can be found from $\tan(\theta_p') = e_p\tan(\theta_p)$. Furthermore, based on geometrical assumptions, the distance $\overline{OQ}$ follows $\overline{OQ} = \left[\frac{2r_{str}}{\sin(\theta_p)} + r_L\right]/\cos(\theta_p')$.

Therefore, by combining the equations above, $\overline{OP}$ can be calculated by $\overline{OP} = 2[r_L\sin(\theta_p) + 2r_{str}]/\sin(2\theta_p)$. The lengths of L_1 and L_2 can also be calculated as $L_1 = 2r_{str}\cot(\theta_p)$ and $L_2 = r_L\cos(\theta_p)$; Thus, the required lengths for the powder stream L_{str} and laser beam cylinders L_L are, respectively,

$$L_{str} = \overline{OP} + L_1 + L_2 = \frac{[r_L\sin(\theta_p) + 2r_{str}]\cdot[3 + \cos(2\theta_p)]}{\sin(2\theta_p)}, \tag{24}$$

$$L_L = \overline{OP}\sin(\theta_p) = \frac{r_L\sin(\theta_p) + 2r_{str}}{\cos(\theta_p)}. \tag{25}$$

Whereas when $2r_{str}/\sin(\theta_p) < r_L$, the traveling distance $\overline{OP}$ follows $\overline{OP} = 2[r_L\sin(\theta_p) - 2r_{str}\cos(2\theta_p)]/\sin(2\theta_p)$, and $L_2 = 2r_{str}\cot(\theta_p)$. Therefore, the required lengths for powder stream and laser beam cylinders are, respectively,

$$L_{str} = \overline{OP} + L_1 + L_2 = \frac{2[r_L\sin(\theta_p) + 2r_{str}]}{\sin(2\theta_p)}, \tag{26}$$

$$L_L = L_{str}\sin(\theta_p) = \frac{r_L\sin(\theta_p) + 2r_{str}}{\cos(\theta_p)}. \tag{27}$$

If the calculated length of the powder or laser cylinder exceeds the experimental length, the experimental values are considered.

An estimation of $v_p = 5.12$ m·s^{-1} for the velocity of powder particles is derived from the experimental diameter of the powder flow on the surface (depicted in Fig. 12b) and the experimental flow rate of the carrier gas. The time needed for particle generation within the powder stream is

$$t_{pg} = \frac{L_{str}}{|\vec{v_p}|}. \tag{28}$$

Therefore, the number of particles generated for each diameter size can be determined by

$$n_{p,i} = round(c_{atten}\dot{n}_{p,i}t_{pg}), \tag{29}$$

where c_{atten} is the model constant, set equal to the magnitude of the particle velocity, $|\vec{v_p}|$, in this study. To statically model the powder stream, the azimuthal and axial distances of each powder particle to the central axis of the powder stream (represented by a cylinder) are randomly chosen, while the radial distance is selected based on a Gaussian distribution with a standard deviation of $r_{str}/2$. The horizontal component of the position of the particles bouncing from the surface is calculated by mirroring the horizontal component of the position of particles in the dark blue region in Fig. 7a. This mirroring is done with respect to the plane passing the point where the particle collides with the surface and is perpendicular to the x-axis. On the other hand, the vertical component of the position of the bounced particle is obtained by multiplying the restitution coefficient, e_p, by the vertical component of the particle's position before its collision with the surface.

In the model, the laser beam intensity profile is characterized by the laser power and the normalized distribution of laser energy density. Powder particles obstruct the laser beam in the form of circular "shadows" in the energy density profile. To minimize the effect of a large numerical grid size in the laser energy density profile on the calculated attenuation coefficient, the number of the initial energy density points of the laser profile is increased sufficiently through interpolation. Next, the laser beam intensity profile and powder particle stream "configuration" (shown in Fig. 7c, and described above) is rebuilt repetitively, where a counter, $N_{shaded,i}$, is specified for each laser energy density point to track the number of times powder particles shadow that point among repetitions, N_{iter}. A point can be shaded only once at each repetition. The attenuated energy density factor for each density point is then calculated by averaging its counter over repetitions, which reads

$$EDF_{atten,i} = \left(1 - \frac{N_{shaded,i}}{N_{iter}}\right) EDF_i. \tag{30}$$

Fig. 8 shows the averaged attenuated energy density profiles corresponding to the experimentally measured circular (top-hat) and square beam shapes with uniform intensity profiles considered in this study; see Fig. 10 in Section 4.

Finally, the overall laser energy attenuation coefficient is calculated as

$$\alpha_{atten} = 1 - \frac{\sum_{i=1}^{N_{lp}} EDF_{atten,i}}{\sum_{i=1}^{N_{lp}} EDF_i}. \tag{31}$$

For circular and square intensity profiles, the laser energy attenuation coefficients, α_{atten}, at a mass flow rate of 2.5 g·min^{-1} for powder stream, are found to equal 14.6% and 12.7%, respectively. The radius of the circular laser spot and the width and length of the square laser spot are chosen identically in the present study, resulting in identical laser-material interaction times. However, it should be noted that the laser spot surface area of the square beam is 21.5% larger than that of the circular beam, while the peak intensity of the unattenuated circular beam profile is 21.5% higher than that of the square beam. Since powder particles are mostly concentrated at the center line of the powder stream, mostly interacting with the front center of the laser beam, they can attenuate the energy of the circular beam more compared to the square beam having the energy dispersed over a larger area. This results in only a 1.9% difference between the attenuation coefficients corresponding to the circular and square laser beams. However, the intensity of the attenuated circular laser beam is still much higher (around 19.6% on average) than that of the square beam.

The present attenuation model is developed for off-axis powder streams; nevertheless, it can be readily extended to accommodate co-axial or other configurations of powder streams relative to the laser beam. An assumption is made regarding uniform particle velocities, but the present model can be expanded to incorporate a distribution of particle velocities along the cross-section of the powder stream. Also, while it is postulated that the powder stream intersects the laser beam at the substrate's surface, the model can be readily expanded to account for a powder stream having an axis that intersects the surface ahead of (or behind) the optical axis of the laser beam.

3. Numerical implementation

Fig. 9 shows the computational domain employed in the present study, depicting a stationary laser beam, a stationary powder stream, and a moving substrate. A layer of argon gas was modeled on the substrate to track the gas-metal interface.

Hexahedral cells were used to discretize the computational domain, defined in a Cartesian coordinate system. Fig. 9 shows the mesh blocks and the boundary conditions employed in the simulations. An atmospheric pressure of $1.013 \cdot 10^5$ Pa was applied to the boundaries of the gas layer. It was assumed that metal evaporation during the process does not appreciably alter the properties of the gas [74]. Marangoni shear force, capillary force, and vaporization recoil pressure were applied to the gas-metal interface. The heat induced by absorbed laser energy and thermal dissipation caused by convection, radiation, and evaporation were applied as a surface heat flux. A 293 K initial temperature was considered throughout the computational domain, including the gas, the substrate material and the powder particles emerging from the nozzle. The simulated physical time of the model is 1 s. This time frame allows

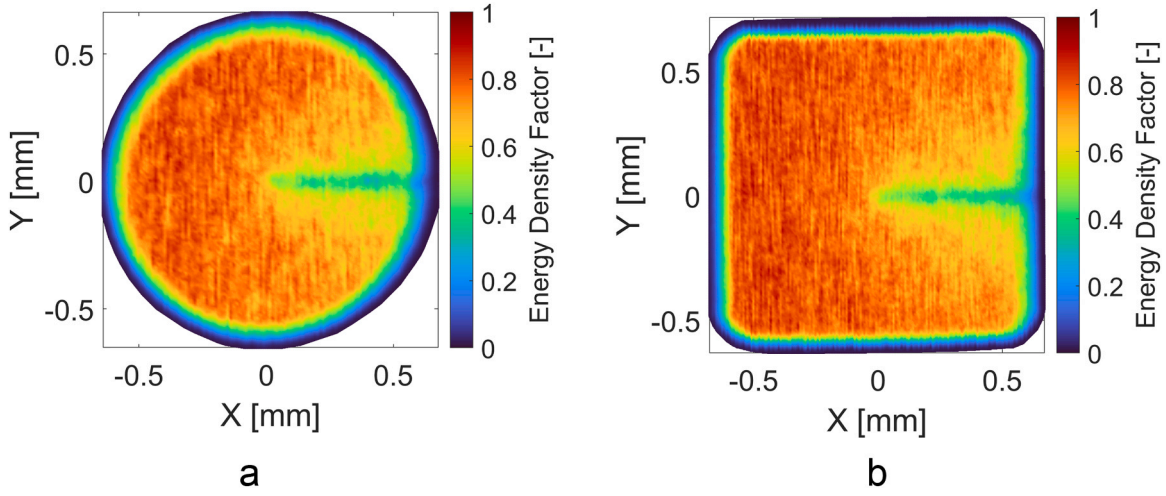

Fig. 8. Normalized energy density profiles of a) circular and b) square laser beams, attenuated by 2.5 g·min^{-1} powder mass rate. The locally reduced intensity "stripe" (green) at the right side of each profile is due to the "shadowing" effect of bouncing particles.

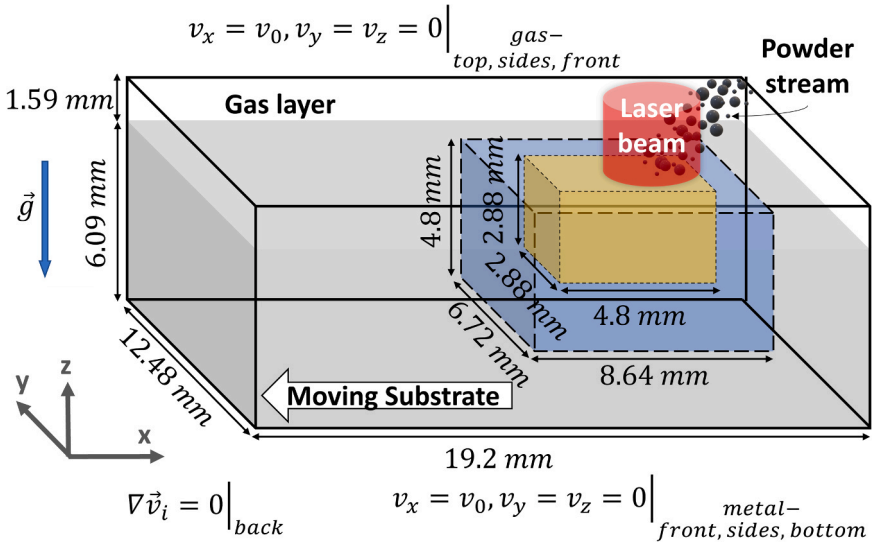

Fig. 9. Schematic of the computational domain, including the gas layer (white), the metal substrate (grey), the gas-metal interface, the laser beam (red) and the powder stream (black circles), three mesh blocks, and boundary conditions related to velocity. The laser beam irradiates the substrate and the particles in the powder stream.

for establishing a quasi-steady-state situation.

The analytical models presented in Section ↱2 were initially employed to calculate various parameters such as the solidification drag coefficient, surface tension coefficient, laser energy absorption coefficient, shape factor, generation rate, number density, and distribution of powder particles, alongside the laser energy attenuation coefficient and the profile of attenuated laser energy density, using MATLAB software [75]. Then, the computational fluid dynamics (CFD) solver Flow-3D 2022-R1 [76] was used to perform the thermal-fluid calculations presented in Section ↱2. Through discretization, the computational domain consists of 478,720 hexahedral cells divided over three mesh blocks to reduce the total number of computational cells in the simulation while having sufficiently fine cells in the melt pool region. In Fig. 9, the smallest mesh block (in green) specified for melt pool thermal-fluid calculations is about twice the size of the melt pool and was discretized by cells with a size of 60 μm. The medium (blue) and the largest (grey) mesh blocks are defined for thermal conduction calculations and were discretized by cells measuring 120 μm and 240 μm, respectively. In regions where mesh blocks overlap, the governing equations were solved in the mesh block with a finer cell size. A symmetry boundary condition was applied at the interface connecting these mesh blocks, and the physical quantities in the solid state at the interface were transferred through three-dimensional interpolation. This scenario is equivalent to the stationary substrate and moving laser beam, where a high-resolution mesh block moves with the laser beam, allowing for accurate and efficient calculation of the local thermal-fluid behavior of the moving melt pool, as detailed in [77]. The generalized minimal residual (GMRES) technique [78] and the generalized conjugate gradient (GCG) algorithm [79] were employed to solve the system of conservation equations implicitly [35]. The first-order upwind differencing method [35] was applied to calculate momentum advection and heat transfer, while the volume of fluid advection was approximated using the split Lagrangian method [35]. Regarding the internal energy, the transport equations were solved using first-order advection [35]. The time step in the simulations was adjusted such that the fluid, free surface, and diffusion of quantities (such as mass and heat) are limited to one cell per time step, resulting in a variable time step [34]. The simulations are executed in parallel on a workstation with 16 GB of memory and 16 cores of an AMD Ryzen Threadripper 3970X 3.70 GHz processor. A typical simulation was completed in less than 4 days.

4. Experimental setup

DED-LB experiments were performed to validate the present model. As a laser source, a Yb:YAG disk laser (TruDisk 10001 of Trumpf GmbH &Co, Germany) emitting an Infrared (IR) laser beam (wavelength of 1030 nm), a laser power of 600–700 W, and a beam parameter product (BPP) of 2 mm·mrad were used. The laser beam was transported to the focusing optics by three user-selectable optical transport fibers. One of the fibers had a circular core with a diameter of 600 μm, resulting in a circular beam shape with a uniform intensity profile, referred to as top-hat, in the focal plane. The second fiber had a square core of 620·620 μm^2, resulting in a square beam shape with a uniform intensity profile in the focal plane. The third fiber had a circular core of 100 μm diameter and an additional ring core of 400 μm in diameter, of which only the ring was used, resulting in a uniform ring-shaped intensity profile. The laser beam emitted from the optical fiber was focused by a BEO D70 focusing head (Trumpf GmbH & CO, Germany) consisting of a 200 mm collimator and focusing lenses with user-selectable focal lengths of 400 mm (for the square and circular beams) and 600 mm (for the ring-shaped beam). This resulted in a 1.2 mm laser beam diameter for the circular and ring-shaped spots and a 1.2 mm side length for the square-shaped spot. A beam profiler (FocusMonitor, Primes GmbH, Germany) was used to measure the intensity profiles in the focal plane, illustrated in Fig. 10. These intensity profiles are imported to the thermal-fluid model as the initial intensity profiles before energy attenuation. To move the laser beam relative to the substrate, the focusing head was mounted on a 6-DOF robot (ABB AG IRB-2600M2004). The focusing head was positioned so the laser beam was perpendicular to the substrate's surface. The focusing head, nozzles and substrate are shown in Fig. 11.

The substrate was an AISI 316 L stainless steel plate (250·100·10 mm^3). Also, AISI 316 L stainless steel particles (Oerlikon Metco 41 C) were employed as powder material. The particle size distribution (PSD) by mass was measured using the sieving technique. Non-spherical particles pass through sieving filters based on their smallest diameters. To account for the size of non-spherical particles, the equivalent particle size, as shown in Fig. 12a, was determined by averaging the current and next levels of the hole diameter in the sieving filter. A Twin-150 powder feeder (Oerlikon Metco AG) supplied the powder carried by argon gas (2.5 $NL{\cdot}min^{-1}$) through an off-axis powder nozzle (OFF-AXIS-F-1.5, Fraunhofer ILT, Germany) with a 1.5 mm inner diameter, at a 70° incidence angle relative to the horizontal, see Figs. 11

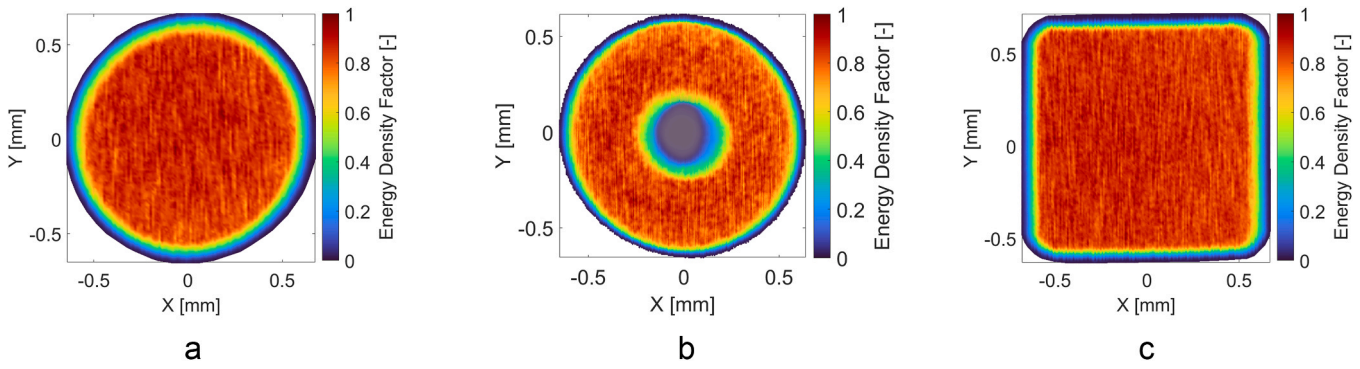

Fig. 10. Normalized laser beam energy density profiles measured experimentally.

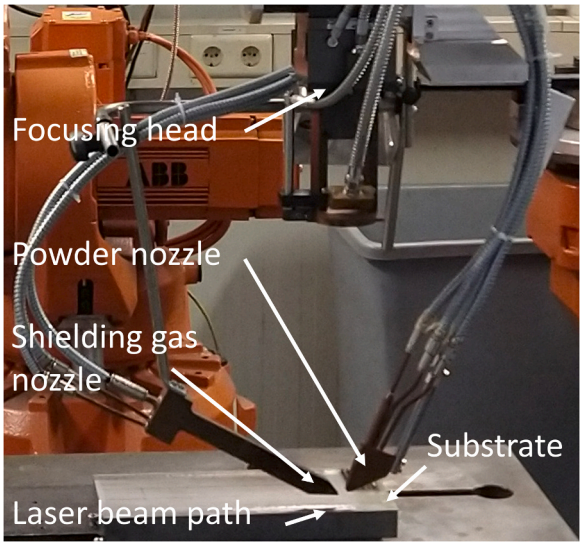

Fig. 11. Photograph of the laser beam focusing head, powder and shielding gas nozzles, the robot (orange) and the substrate in the DED-LB experimental setup.

and 12b. The nozzle was fixed to the side of the focusing head. The resulting particle stream collided with the substrate surface and had a horizontal diameter of 3.22 mm, which was derived from Fig. 12b. Also, argon as a shielding gas with a density of 1.6 kg·m^{-3}, exiting from a second nozzle (Fraunhofer ILT, Germany), was used to protect the melt pool and hot deposited tracks against oxidation with a flow rate of 20 NL·min^{-1} and a velocity of 3.33 m·s^{-1}, incident at a 25° angle, see Fig. 12b.

Two types of experiments were performed: laser melting, in which no powder is fed to the melt pool, and laser-DED. Laser melting was conducted with a laser power set at 700 W and a laser beam scanning speed of 20 mm·s^{-1}. In the laser-DED experiment, a laser power of 600 W and a speed of 5 mm·s^{-1} were used with a powder mass flow rate of 2.5 g·min^{-1}.

After cutting and polishing (LaboPol-60, Struers ApS, Denmark), the resulting samples were etched using a solution composed of 100 mL HCl, 100 mL H_2O, and 10 mL HNO_3 at 310 K. Finally, the samples were mounted in Bakelite for digital imaging using an optical microscope (VHX 7000, Keyence, Japan).

5. Results and discussion

5.1. Model validation

This section focuses on the validation of the present thermal-fluid model in terms of its reliability and accuracy. First, the simulation results of laser melting—i.e., without injection of powder particles into the laser-induced melt pool— are compared to experimental results. Next, the simulation results of laser-DED are compared to experiments in which powder is injected into the melt pool.

Fig. 13 shows a comparison between the shape and dimension of a

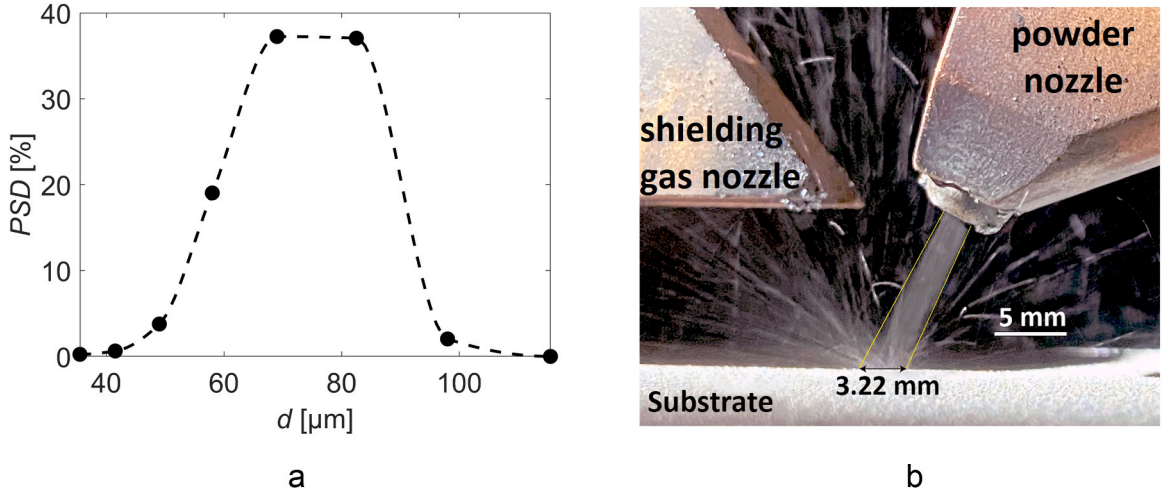

Fig. 12. a) Particle size distribution (PSD [%]) (derived from mass) of Oerlikon Metco 41 C powder particles, measured by sieving. The dashed curve serves as a visual aid. b) Photograph of powder particles exiting the powder nozzle (right) carried by argon gas. A second nozzle (left) supplies argon to shield the melt pool and the hot deposited track (bead) from oxidation.

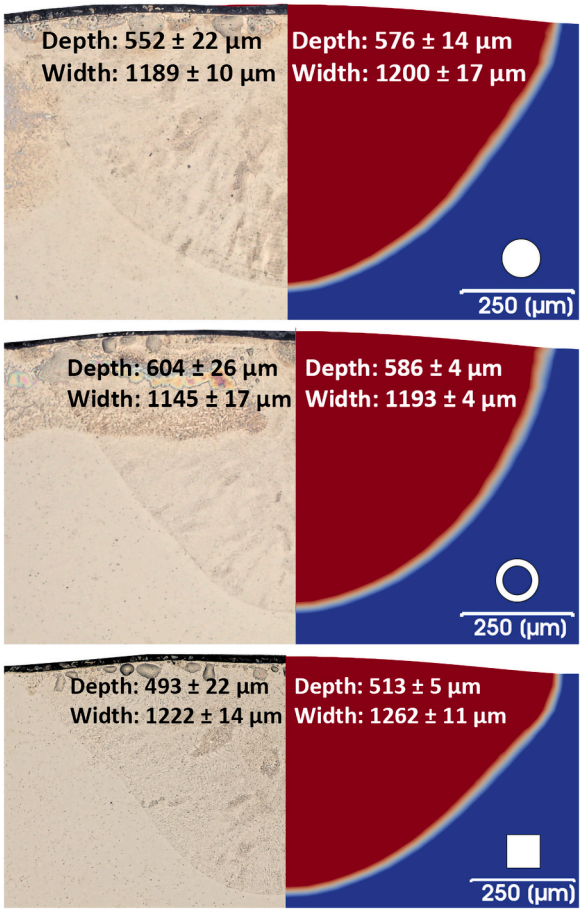

Fig. 13. Comparison between the numerical (right) and experimental (left) transverse cross-sections of laser-melted tracks induced by circular, ring, and square-shaped intensity profiles. All tracks were obtained at 700 W laser power with a 20 mm·s^{-1} beam scanning speed. The blue area in the numerical cross-sections corresponds to the region without melting, the red area to the fusion region, and the white zone to the mushy zone. The laser spot shapes are indicated above the scale bar.

Table 5
Prediction errors by the numerical model of the dimensions (width, depth, height) of the fusion zone, when compared to experimental results, for the three laser beam intensity profiles.

	Numerical error		
Beam shape (uniform intensity profile)	**Depth**	**Width**	**Height**
	Laser melting		
Circular	4.3%	0.9%	N.A.
Square	4.0%	3.2%	N.A.
Ring	-2.9%	4.1%	N.A.
	DED-LB		
Circular	-7.7%	0.8%	-1.6%
Square	8.4%	4.1%	-1.6%
	DED-LB, only attenuated laser power		
Circular	-5.8%	1.3%	-2.8%
	DED-LB, unattenuated laser power and intensity profile		
Circular	15.5%	2.2%	-1.1%

cross-section of the melt pools obtained from experiments (left) and numerical simulations (right) for laser melting cases using three different intensity profiles. The numerical cross-sections are associated with the cross-section exhibiting the maximum depth of the melt pool. Table 5 lists the deviation between the melt pool dimensions numerically predicted compared to the experiments. The average errors in predicting the depth and width of the melt pool are only 3.7% and 2.7%, respectively.

Fig. 14 shows a comparison between the experimental (left) and numerical (right) cross-sections of single tracks (beads) of deposited material created by the circular and square-shaped laser beams with uniform intensity profiles. The width and depth of the melt pool are indicated, as is the height of the tracks. The averaged errors in predicting the melt pool depth, width, and height are 8%, 2.4% and 1.6%, respectively. The results of this validation demonstrate the ability of the model to accurately predict the morphology of the deposited layer, even under different laser beam intensity profiles.

5.2. *The effect of powder stream on laser energy attenuation*

Existing literature contains only a few thermal-fluid models of DED-LB that incorporate the powder particle stream [21,36,54,58,80–82]. Nevertheless, these models neglect the impact of the powder particle stream on laser energy attenuation. Fig. 15 shows the computed laser power attenuation coefficient as a function of various powder stream characteristics, including the powder stream incidence angle, θ_p, (relative to the horizontal), powder mass flow rate, $\dot{m}_{src}$, and the apparent cross-sectional diameter, $2r_{str}$. A diameter ($2r_L$) of 1.2 mm was set for the circular laser beam with a uniform intensity profile. The data shown in Fig. 15a indicate that the attenuation coefficient increases with increasing the powder mass flow rate for a constant stream diameter of 2.5 mm. At lower incidence angles (below 30°), the ratio of the attenuation coefficient to the powder mass flow rate shows only a marginal decrease with an increase in the powder mass flow rate, —i.e. it shows a nearly linear correlation. This decrease is attributed to the fact that a particle can block the laser ray from reaching a particle below it, meaning that a particle is shading a (part of a) particle below it. Particularly, at higher incidence angles, this particle overlap intensifies, especially the overlap between the entering and bouncing particles increases, leading to a more pronounced decline in the ratio of the attenuation coefficient to the powder mass flow rate as the powder mass flow rate increases. The impact of increasing the powder mass flow rate on the intensity profile becomes evident when comparing the energy density profiles in Fig. 8a for a flow rate of 2.5 g·min^{-1} and Fig. 16a for a flow rate of 7 g·min^{-1}. A higher flow rate in the latter leads to more particles shading the laser beam, resulting in greater attenuation across the entire laser beam intensity profile.

Fig. 15b shows the dependency of the attenuation coefficient on the incidence angle for different powder mass flow rates. At low incidence angles (below 30°), a plateau is observed indicating a slight change (smaller than 10%) in the attenuation coefficient. However, at higher incidence angles, the attenuation coefficient experiences a noteworthy increase with raising the incidence angle, particularly at higher flow rates. Elevating the incidence angle enlarges the overlapping region between the entering and bouncing powder streams and the laser beam, representing a greater number of particles shading the laser beam. This is readily apparent when comparing the attenuated energy density profiles at a high incidence angle (70°) in Fig. 8a and at a lower incidence angle (30°) in Fig. 16b. Moreover, in Fig. 15c, the attenuation coefficient is compared for various apparent diameters of the powder stream at a constant incidence angle of 50° and different powder mass flow rates. The attenuation coefficient increases with the apparent diameter until the latter reaches a value close to the laser beam diameter. This is because an increase in the stream diameter leads to the dispersion of powder particles, reducing the shading events of particles by other particles and enhancing participation in energy attenuation. After reaching a peak value, a subsequent increase in the powder stream diameter leads to a decrease in the attenuation coefficient, primarily due to some particles being positioned outside the laser beam. However, owning to the normal distribution of powder particles, the majority concentrate at the center line of the powder stream, leading to only a marginal decrease in attenuation. This pattern persists for all incidence

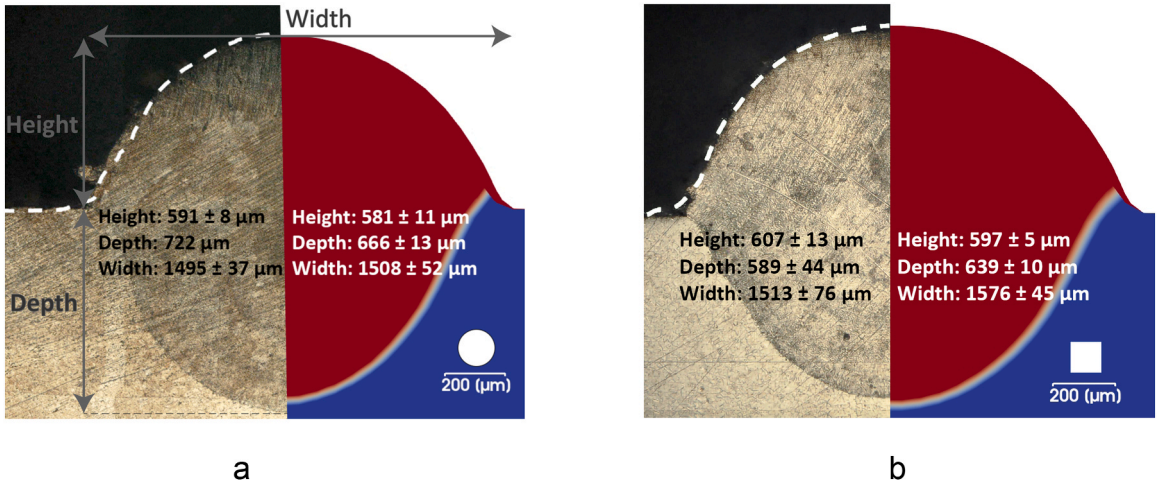

Fig. 14. Comparison between the experimental (left) and numerical (right) transverse cross-sections of single tracks created by DED-LB using (a) circular and (b) square-shaped laser beams with uniform intensity profiles at 600 W laser power, with a 5 mm·s^{-1} scanning velocity and a 2.5 g·min^{-1} powder addition rate. The white dashed curve represents the averaged height profile for multiple experimental cross-sections.

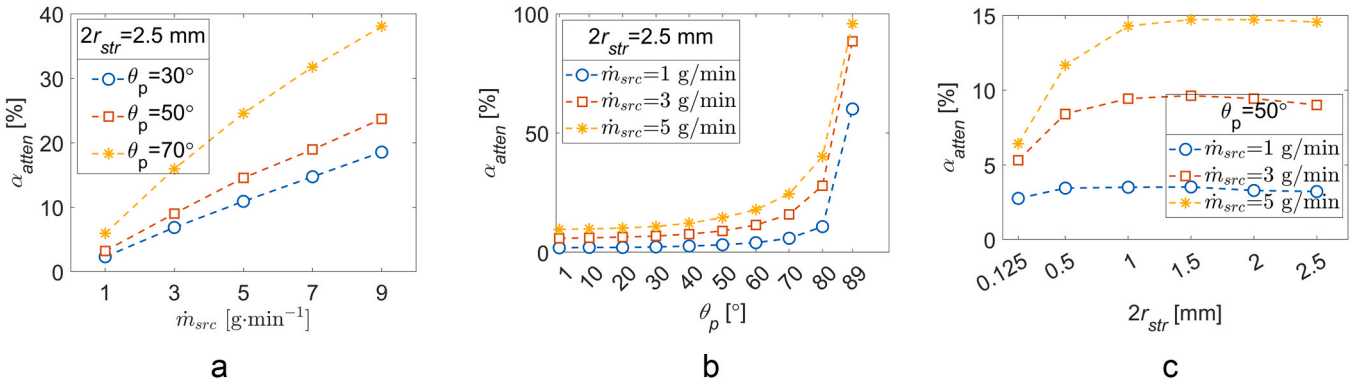

Fig. 15. Calculated laser energy attenuation coefficient, α_{atten}, of the uniform circular laser beam intensity profile (top-hat) with a diameter of 1.2 mm, as a function of different characteristics of the powder particle stream, including a) mass flow rate, $\dot{m}_{src}$, b) the incidence angle to the horizonal, θ_p, and c) the apparent diameter of the powder stream ($2r_{str}$).

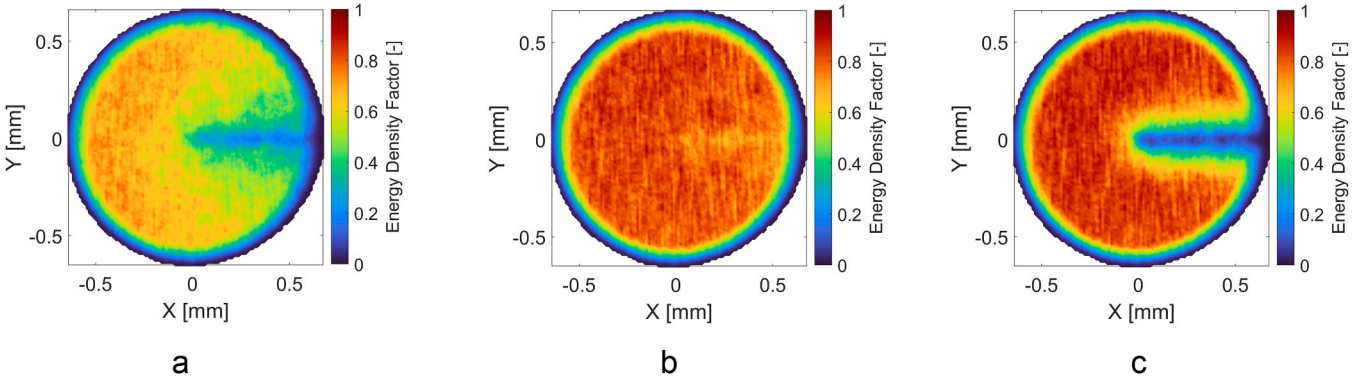

Fig. 16. Attenuated normalized energy density profiles of the uniform circular intensity profile of a laser beam with a 1.2 mm diameter, interacting with a powder stream characterized by mass flow rate ($\dot{m}_{src}$,), the incidence angle to the horizonal, θ_p, and c) the apparent diameter of the powder stream ($2r_{str}$).

angles. This can be verified by comparing the attenuated energy density profile for a narrow powder stream (Fig. 16a) with that for a wide stream (Fig. 8a). The corresponding attenuation coefficient to the former is 11.4%, whereas for the latter, it is 14.6%, compared to the attenuation coefficient of 15.1% for a stream with a diameter of 1.2 mm.

These findings indicate that laser energy attenuation is minimized under conditions of small powder mass flow rates, reduced powder stream incidence angles (< 30°), and smaller apparent diameters of the powder stream relative to the laser beam diameter.

5.3. The effect of attenuation in laser power and intensity profile

In DED-LB simulations, it is critical to consider the phenomenon of laser energy attenuation, as described in Section ↱2. The attenuation of

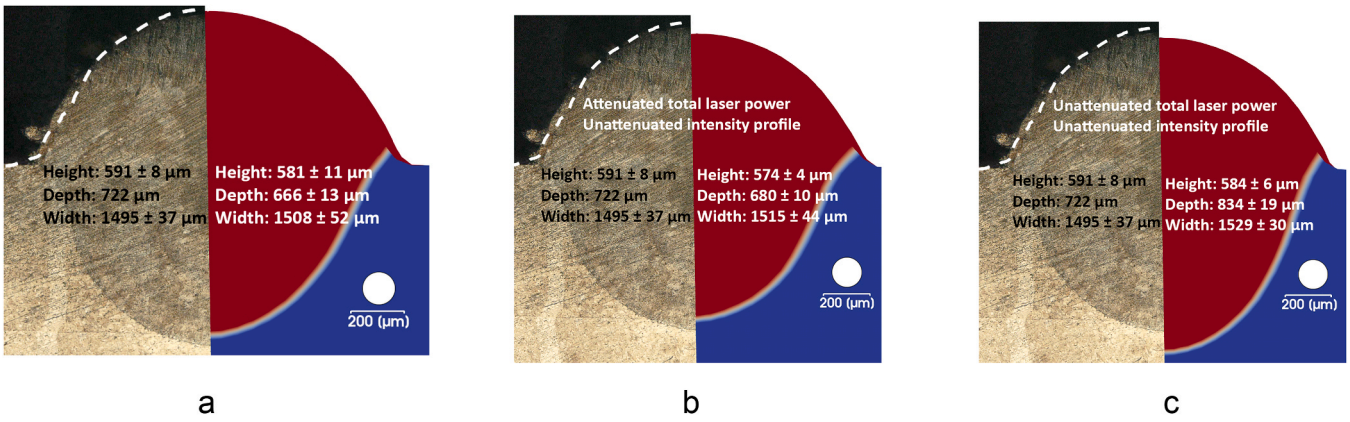

Fig. 17. Experimental (left) and numerical (right) transverse cross-sections of the deposited material induced by the circular laser beam with a uniform intensity profile at 600 W laser power, 5 mm·s^{-1} beam scanning velocity, and 2.5 g·min^{-1} powder addition rate. (a) Numerical simulations incorporating attenuation in laser *power* and energy density *profile*. (b) Numerical simulations considering attenuation in laser power, while excluding energy density attenuation. (c) Numerical simulations without attenuation in laser power and intensity profile.

laser energy can significantly impact the resulting melt pool dimensions and shape. To illustrate the effects of powder-induced laser energy attenuation, simulations were conducted which did not incorporate attenuation of the laser power and/or intensity profile of the beam, as discussed with respect to Fig. 8. To this end, Fig. 17 shows the numerical (right) and experimental (left) transverse cross-sections of the deposited

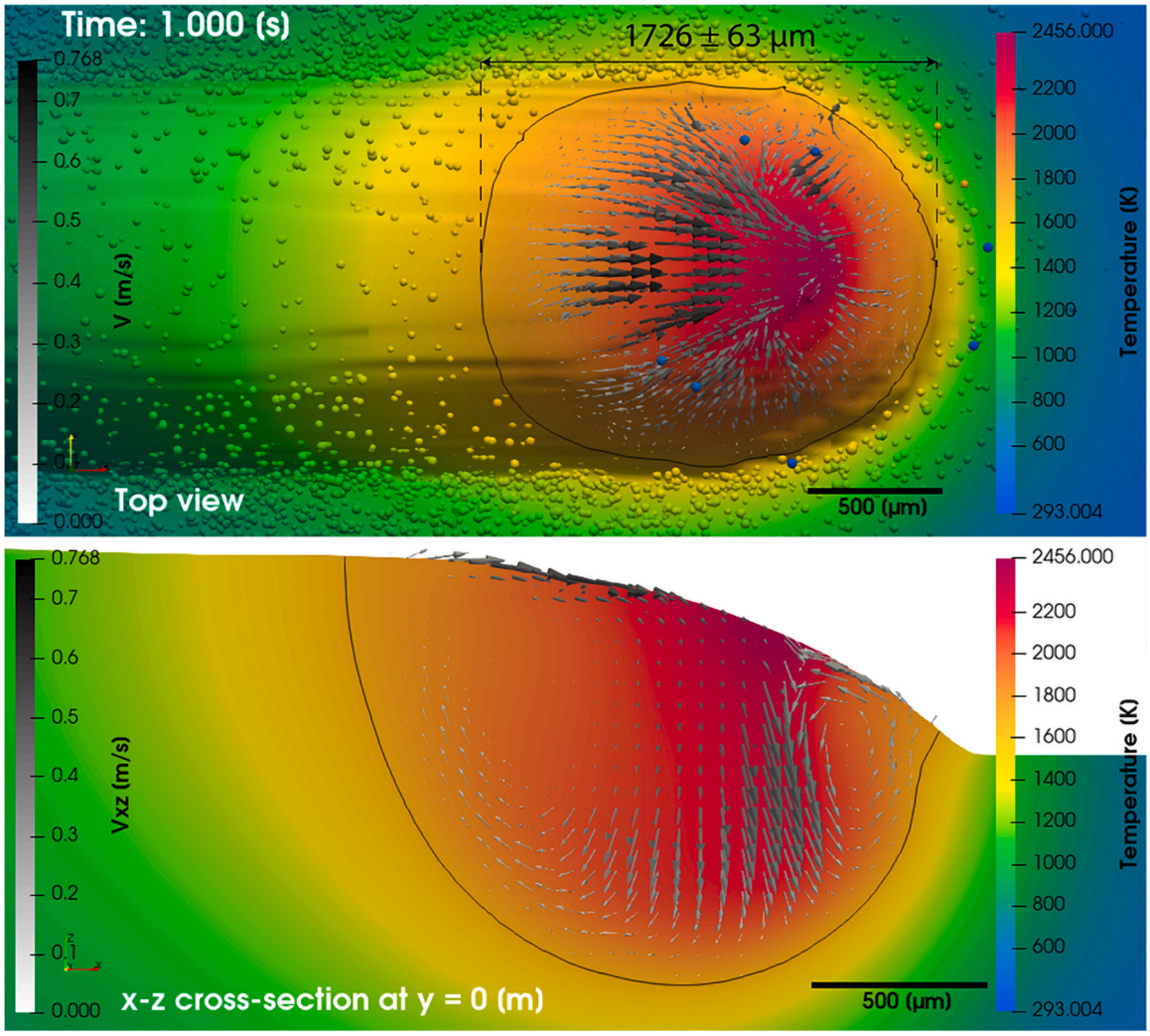

Fig. 18. Numerical results depicting fluid velocity (dark arrows) profile and temperature distribution in the melt pool, induced by the uniform circular laser beam intensity profile with 600 W power, 5 mm·s^{-1} scanning velocity and a powder mass flow rate of 2.5 g·min^{-1}. The continuous black curve indicates the solidus temperature as the melt pool's boundary.

material created by the circular laser beam with a uniform intensity profile. The numerical simulation results shown in Fig. 17a include attenuation of the total laser power and the intensity profile. In Fig. 17b, laser power attenuation is included, but the attenuation of the energy density profile is neglected. Fig. 17c shows similar graphs, but the attenuation in the laser power and the intensity profile was not considered in the numerical simulations. The corresponding error values are reported in Table 5.

The significance of considering laser energy attenuation when simulating DED-LB is evident when comparing the results shown in Fig. 17. Compared to the simulation results in Fig. 17a, neglecting attenuation of the intensity profile (Fig. 17b) results in simulation deviations of -1.2%, 2.1%, and 0.5% in height, depth and width, respectively. Fig. 18 shows the numerical results of the top view and the longitudinal cross-section of a deposited track generated by the circular laser beam with a uniform intensity profile, attenuated in both the power and the intensity profile, while Fig. 19a shows comparable results for the uniform circular laser beam with only its power attenuated. The peak temperature is observed at the front of the melt pool, directly under the forefront of the laser beam. These peak temperatures are 2456 K in Fig. 18 and 2462 K in Fig. 19a. These deviations occur because neglecting the attenuated intensity at the front of the intensity profile (Fig. 8a) leads to more energy being absorbed at the front of the melt pool, resulting in a slightly higher local temperature at the front. An increase in temperature results in higher energy absorption due to the elevated absorption coefficient. This higher peak temperature results in larger temperature gradients, leading to a higher Marangoni shear stress. This, in turn, induces greater convection, resulting in a deeper melt pool. On the other hand, based on Fig. 3, the higher peak temperature results in lower surface tension, causing the height profile to be less “drawn” or “pulled” to the center of the melt pool, leading to a reduction in the height of the profile. The latter reduces the curvature of the height profile at the center line of the deposited track and disperses more material to the sides of the melt pool. In turn, this slightly increases the width of the melt pool.

Furthermore, neglecting the attenuation in both laser power and intensity profile (Fig. 17c) results in even larger prediction errors and deviations (see Table 5) compared to experimental and numerical cross-sections in Fig. 17a. In this case, simulation deviations of 0.5%, 25.2%, and 1.4% in height, depth and width, respectively, are obtained compared to the simulation results in Fig. 17a. Fig. 19b shows the numerical results of the top view and cross-sections of a deposited track formed by the uniform circular laser beam intensity profile, with no attenuation in either the power or intensity profile. In this case, the peak temperature is 2565 K, which surpasses the peak temperatures observed in cases where attenuation was factored in. This overestimation of the melt pool temperature profile, and thus the dimensions (significantly in depth), occurs because neglecting the attenuation phenomenon leads to an overestimation of the absorbed laser energy. The overestimated peak temperature is associated with larger temperature gradients, resulting in a higher Marangoni shear stress. This, in turn, induces greater convection, resulting in a deeper melt pool. As the melt pool width primarily depends on the size of the laser spot, a 14.6% overestimation in absorbed energy only yields a marginal 1.4% increase in melt pool width. However, the wider melt pool facilitates embedding more particles, contributing to an increase in the height of the clad profile. This compensates for the reduction in height due to lower surface tension at elevated temperatures, resulting in the profile being less drawn toward the center of the melt pool.

5.4. The effect of laser beam intensity profile

The size of the melt pool is primarily influenced by the absorbed laser energy, while the laser beam intensity profile controls the temperature distribution, thereby affecting the melt pool shape. Laser power attenuation for a square-shape laser beam was found to be $\alpha_{atten} = 12.7\%$, which is less than that of a circular beam ($\alpha_{atten} = 14.6\%$). This allows the melt pool induced by the square beam to absorb more heat. Fig. 20 shows the numerical results of the top view and the longitudinal cross-section of the melt pool induced by the uniform square laser beam intensity profile. It can be concluded from the simulation results shown in Figs. 18 and 20 that the square-shaped profile creates a 12.5% larger melt pool volume than the circular-shaped profile for identical processing parameters due to the lower power attenuation coefficient and larger irradiated surface of the square profile. The square laser profile creates a melt pool with a volume of 1.55 mm^3 compared to the circular-

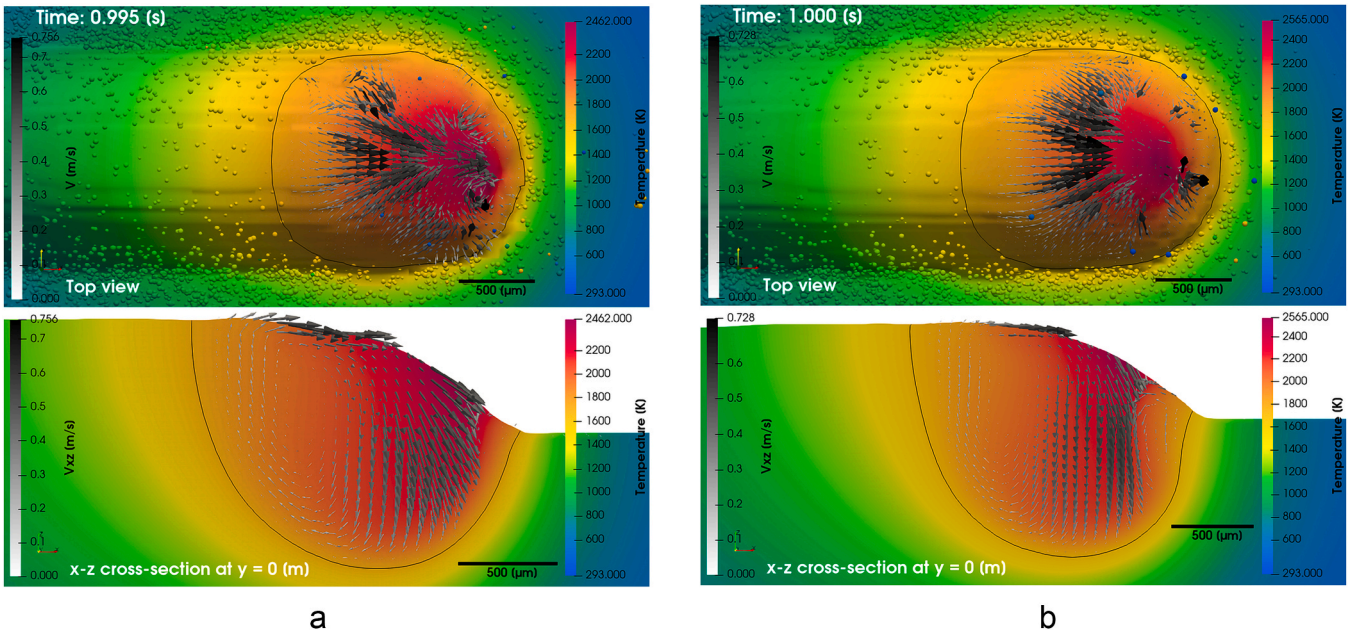

Fig. 19. Numerical results of the fluid velocity (dark arrows) profile and temperature distribution of the melt pool induced by a uniform circular laser beam intensity profile, a) only attenuated in power, and b) unattenuated in both power and intensity profile. A scanning velocity of 5 $mm{\cdot}s^{-1}$, a power of 600 W and a powder mass flow rate of 2.5 $g{\cdot}min^{-1}$ were used. The continuous black curve indicates the solidus temperature as the melt pool's boundary.

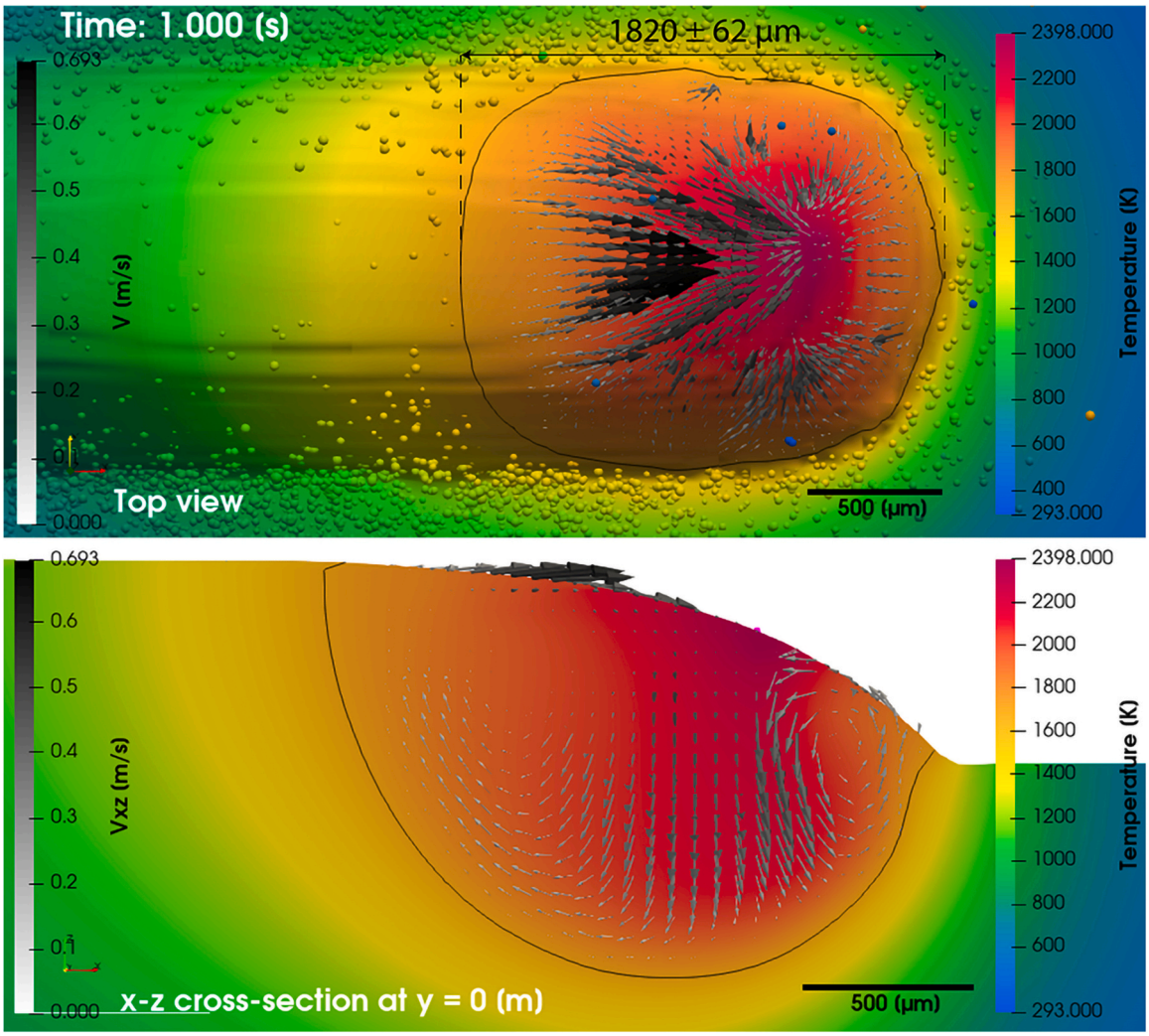

Fig. 20. Numerical results of fluid velocity (dark arrows) profile and temperature distribution within the melt pool induced by the uniform square laser beam intensity profile with 600 W power, 5 mm·s^{-1} scanning velocity and a powder mass flow rate of 2.5 g·min^{-1}. The continuous black curve indicates the solidus temperature as the melt pool's boundary.

shaped beam with a volume of 1.38 mm^3. Moreover, more input energy on the side boundaries of the pool increases its width. Therefore, the melt pool is wider when using a square-shaped intensity profile (Fig. 14) than when using a circular profile. A larger melt pool, especially in terms of width and length, leads to a greater influx of particles joining the melt pool, contributing to a larger height of the clad profile, as achieved in the case of the square beam. Furthermore, the square-shaped laser beam, with a surface area 25.5% larger than the circular beam, coupled with greater energy deposition on the melt pool surface (attributed to a lower attenuation coefficient), results in the generation of a longer melt pool along the direction of the laser beam movement compared to the circular profile. As can be concluded from Figs. 18 and 20, the melt pool generated by the square beam shape has a length of 1820 µm, which is 4.7% longer than the melt pool length of 1726 µm induced by the circular profile.

The melt pool induced by the uniform circular profile (Fig. 18) shows a higher peak temperature of 2456 K at the surface of the melt pool due to a higher energy intensity, compared to the peak surface temperature of 2398 K induced by the uniform square profile (Fig. 20). Conversely, elevated temperatures lead to increased energy absorption, driven by a higher absorption coefficient. A higher peak temperature implies more significant temperature gradients across the melt pool surface, which, in turn, can contribute to an increase in the Marangoni shear stress, convection and fluid velocity, resulting in more noticeable heat and fluid flow penetrating towards the bottom of the melt pool. The maximum fluid velocity in the melt pool induced by the circular profile is 0.768 m·s^{-1}, faster than the maximum fluid velocity of 0.693 m·s^{-1} induced by the square profile. As a result, the circular profile induces a 11.5% deeper melt pool than the square profile, as shown in Fig. 14.

Dimensionless numbers can provide insights into fluid flow patterns and heat transfer during deposition [20]. The Peclet number (Pe) allows for the evaluation of the competition between thermal conduction and convection within the melt pool [20,83], and is proportional to the temperature gradient across the melt pool [84]. Pe number can be expressed as [54]

$$\mathrm{Pe} = \frac{\rho C_p L_c v_{peak}}{k}, \tag{32}$$

where L_c is the characteristic length as the melt pool length, v_{peak} is the peak velocity within the melt pool. Specifically, when Pe is less than 1, the heat transfer is predominantly governed by thermal conduction or diffusion, while a Pe value exceeding 1 indicates the dominance of Marangoni thermal convection [83,85–87].

Accordingly, the Peclet numbers associated with melt pools induced by the uniform circular and square laser beams are 207 and 197, respectively. As a result, due to the Pe number being larger than 1 for both laser beams, the depth of the melt pool is predominantly

determined by the transfer of heat and mass by the downward fluid flow (i.e., convection), with the impact of heat conduction being less significant on the depth of the melt pool. The Peclet number for the melt pool formed by the uniform circular beam is higher than that for the square one. This highlights the enhanced role of fluid flow in convection for the former beam shape.

Another notable dimensionless number is the Marangoni number (Ma), which quantifies the effect of the Marangoni shear stress on fluid behavior [20]. The Marangoni number is closely tied to surface tension variations resulting from temperature differences, influencing the overall dynamics of the melt pool and affecting the fluid velocity within the melt pool [87]. This number represents the ratio of surface shear stress to viscous force [20]. Ma can be calculated as [88,89,90].

$$\mathrm{Ma} = \frac{d\gamma}{dT}\frac{\rho C_p L_c \left(T_{peak} - T_s\right)}{\mu k}, \tag{33}$$

where T_{peak} is the peak temperature of the melt pool [83]. ρ, C_p, μ and k are determined at the solidus temperature [20,85]. When Ma exceeds 1, the Marangoni effect dominates over viscous forces, significantly impacting fluid flow patterns [20].

The Marangoni numbers corresponding to melt pools induced by the uniform circular and square laser beams are calculated as $3.07{\cdot}10^7$ and $3.01{\cdot}10^7$, respectively, proving the dominance of the surface shear stress over viscous forces for both melt pools, with an advantage for the uniform circular beam. Specifically, the higher temperature difference induced by the uniform circular laser beam makes the Marangoni force stronger due to the higher surface tension, leading to faster fluid flow in the melt pool [85].

6. Conclusions and future work

A high-fidelity multi-phase thermal-fluid model was presented, aiming at investigating the influence of laser beam intensity profile on melt pool behavior (shape, dimension, fluid dynamics, temperature distribution) in directed energy deposition (DED-LB). The proposed approach introduces a novel laser energy attenuation model that accounts for the shading effect of powder particles on laser power and intensity profiles reaching the substrate. Unlike existing models, the proposed approach more accurately captures the complex interplay between powder particles and laser energy distribution, comprehensively integrates the variable material properties and process parameters, enhancing understanding and control of process dynamics in laser based metal additive manufacturing, and representing a significant advancement in predictive thermal-fluid modeling for additive manufacturing processes. The numerical model was validated by the laser melting and DED-LB experimental results for the three laser beam shapes, namely circular, square, and ring (only in laser melting), characterized by the uniform intensity profile. The following conclusions are derived from the present study:

- In numerical simulations of melt pool behavior in DED-LB, it is critical to account for attenuation in both the laser power and intensity profile due to the flying powder particles. Neglecting attenuation leads to overestimating the locally absorbed laser energy, particularly at the forefront of the melt pool. This can lead to an elevated peak temperature and fluid velocity, and larger melt pool dimensions, notably in depths up to 25%.
- The attenuation coefficient increases with increasing the powder mass flow rate, particularly at elevated powder stream incidence angles to the horizontal, due to the increased particle shading of the laser beam. At lower incidence angles, a marginal decrease in the ratio of attenuation coefficient to flow rate is noted, attributed to particle positioning effects. Additionally, the attenuation coefficient rises with the powder stream diameter until reaching a value close to the laser beam diameter, leading to the peak energy attenuation coefficient. Further increases in diameter result in a decrease in the attenuation coefficient due to particle dispersion.
- Compared to the uniform square laser beam intensity profile, the circular profile concentrates more energy towards the powder stream, leading to increased energy attenuation in the power and intensity profile when interacting with the powder particles and, therefore, a smaller melt pool.
- The shape of the laser beam significantly influences the melt pool behavior in DED-LB. For identical size in terms of the length and width of a square laser beam and the diameter of a circular laser beam, the square-shaped laser beam, with lower power attenuation and a larger irradiation surface, creates a larger melt pool volume compared to a circular beam. The square beam induces a wider and longer melt pool, contributing to a larger height of the clad profile. However, the circular profile generates a higher peak temperature and faster fluid velocity, resulting in a deeper melt pool. The higher Peclet number for the circular beam underscores the heightened role of fluid flow in energy transfer, leading to a deeper melt pool compared to the square beam. Moreover, the higher Marangoni number for the circular beam highlights the dominance of surface shear stress over viscous forces, resulting in faster fluid flow within the melt pool.

Overall, this study demonstrates the accuracy and robustness of the presented model in capturing complex melt pool behavior in DED-LB. This model proves its effectiveness for practical use in optimizing laser-based additive manufacturing processes across diverse materials and geometric configurations.

In future research, the thermal-fluid simulation results will be used to explore the performance of the model with other materials and process parameters and provide a deeper understanding of its capabilities and limitations. In addition, the thermal-fluid simulation results will be used as input to a microstructure model to predict microstructures after (re) solidification of the melt pools induced by various laser beam intensity profiles. Last but not least, the model will be employed to establish an optimized laser intensity profile, focusing on maximizing cooling rates and minimizing temperature gradients, thereby enhancing the temperature profile and induced microstructure.

CRediT authorship contribution statement

Gert-willem R.B.E. Römer: Writing – review & editing, Supervision, Resources, Project administration, Methodology, Funding acquisition. **Amin Ebrahimi:** Writing – review & editing, Writing – original draft, Supervision, Methodology, Formal analysis, Conceptualization. **Martin Luckabauer:** Writing – review & editing, Validation, Supervision, Resources, Methodology, Investigation. **Mohammad Sattari:** Writing – review & editing, Writing – original draft, Visualization, Validation, Software, Resources, Project administration, Methodology, Investigation, Formal analysis, Data curation, Conceptualization.

Declaration of competing interest

The authors declare that they have no known competing financial interests or personal relationships that could have appeared to influence the work reported in this paper.

Data availability

Data will be made available on request.

Acknowledgement

We sincerely thank Prof. Anthony Thornton, Dr. Frieder Semler, and Leon Bremer for their contributions to this study. Dr. Thornton's insightful discussions on particle dynamics principles shaped the

direction of this research. Dr. Semler's guidance and consultation in modeling significantly enhanced the research quality. We are grateful to Leon Bremer for his exceptional support in the laser experiments. Moreover, we would like to highlight Leon Bremer's valuable discussions and insights throughout the course of the project. His thoughtful input and feedback greatly contributed to the interpretation and understanding of the experimental findings.

The study was performed as a component of the Aim2XL program, which is part of the collaborative Partnership Program between the Netherlands Organization for Scientific Research (www.nwo.nl) and the Materials Innovation Institute M2i (www.m2i.nl), and was designated by project number P16–46/S17024i. The authors would like to thank the industrial partners, including the Rotterdam Fieldlab Additive Manufacturing BV (RAMLAB), (www.ramlab.com).

References

[1] D. Svetlizky, M. Das, B. Zheng, A.L. Vyatskikh, S. Bose, A. Bandyopadhyay, J. M. Schoenung, E.J. Lavernia, N. Eliaz, Directed energy deposition (DED) additive manufacturing: physical characteristics, defects, challenges and applications, Mater. Today 49 (2021) 271–295, https://doi.org/10.1016/j.mattod.2021.03.020.

[2] D. Gu, X. Shi, R. Poprawe, D.L. Bourell, R. Setchi, J. Zhu, Material-structure-performance integrated laser-metal additive manufacturing, Science 372 (2021) eabg1487, https://doi.org/10.1126/science.abg1487.

[3] S.M.A. Noori Rahim Abadi, Y. Mi, F. Sikström, A. Ancona, I. Choquet, Effect of shaped laser beam profiles on melt flow dynamics in conduction mode welding, Int. J. Therm. Sci. 166 (2021) 106957, https://doi.org/10.1016/j.ijthermalsci.2021.106957.

[4] A. Ebrahimi, C.R. Kleijn, I.M. Richardson, Numerical study of molten metal melt pool behaviour during conduction-mode laser spot melting, J. Phys. Appl. Phys. 54 (2021) 105304, https://doi.org/10.1088/1361-6463/abca62.

[5] A. Ebrahimi, M. Sattari, A. Babu, A. Sood, G.-W.R.B.E. Römer, M.J.M. Hermans, Revealing the effects of laser beam shaping on melt pool behaviour in conduction-mode laser melting, J. Mater. Res. Technol. 27 (2023) 3955–3967, https://doi.org/10.1016/j.jmrt.2023.11.046.

[6] S.J.L. Bremer, M. Luckabauer, G.R.B.E. Römer, Laser intensity profile as a means to steer microstructure of deposited tracks in directed energy deposition, Mater. Des. 227 (2023) 111725, https://doi.org/10.1016/j.matdes.2023.111725.

[7] K. Partes, G. Sepold, Modulation of power density distribution in time and space for high speed laser cladding, J. Mater. Process. Technol. 195 (2008) 27–33, https://doi.org/10.1016/j.jmatprotec.2007.05.052.

[8] R.L. Higginson, M. Gibson, J. Kell, J. Tyrer, Weld pool shaping and microstructural control using novel computer generated holographic optic laser welding of steel and stainless steel, Mater. Sci. Forum 638–642 (2010) 3673–3678, https://doi.org/10.4028/www.scientific.net/MSF.638-642.3673.

[9] R.L. Higginson, M. Blackmur, M. Gibson, J. Tyrer, Grain size control in the weld pool and heat affected zone using holograms, Mater. Sci. Forum 715–716 (2012) 340–345, https://doi.org/10.4028/www.scientific.net/MSF.715-716.340.

[10] S. Shang, D. Wellburn, Y.Z. Sun, S.Y. Wang, J. Cheng, J. Liang, C.S. Liu, Laser beam profile modulation for microstructure control in laser cladding of an NiCrBSi alloy, Surf. Coat. Technol. 248 (2014) 46–53, https://doi.org/10.1016/j.surfcoat.2014.03.018.

[11] S. Liu, F. Kong, S. Shi, R. Kovacevic, Study of a hollow laser beam for cladding, Int. J. Adv. Manuf. Technol. 73 (2014) 147–159, https://doi.org/10.1007/s00170-014-5763-1.

[12] S. Liu, P. Farahmand, R. Kovacevic, Optical monitoring of high power direct diode laser cladding, Opt. Laser Technol. 64 (2014) 363–376, https://doi.org/10.1016/j.optlastec.2014.06.002.

[13] N.J. Goffin, R.L. Higginson, J.R. Tyrer, The use of holographic optical elements (HOE's) to investigate the use of a flat irradiance profile in the control of heat absorption in wire-fed laser cladding, J. Mater. Process. Technol. 220 (2015) 191–201, https://doi.org/10.1016/j.jmatprotec.2015.01.023.

[14] E. Govekar, A. Jeromen, A. Kuznetsov, G. Levy, M. Fujishima, Study of an annular laser beam based axially-fed powder cladding process, CIRP Ann. 67 (2018) 241–244, https://doi.org/10.1016/j.cirp.2018.04.082.

[15] J. Kelbassa, A. Gasser, J. Bremer, O. Pütsch, R. Poprawe, J. Henrich Schleifenbaum, Equipment and process windows for laser metal deposition with coaxial wire feeding, J. Laser Appl. 31 (2019) 022320, https://doi.org/10.2351/1.5096112.

[16] A. Ebrahimi, MoltenMetal Oscillatory Behaviour: in Advanced Fusion-basedManufacturing Processes, Delft University of Technology, 2022, https://doi.org/10.4233/UUID:06FF0B5E-D5DA-4149-A90F-62064C29F238.

[17] A.J. Pinkerton, An analytical model of beam attenuation and powder heating during coaxial laser direct metal deposition, J. Phys. Appl. Phys. 40 (2007) 7323–7334, https://doi.org/10.1088/0022-3727/40/23/012.

[18] X. Guan, Y.F. Zhao, Modeling of the laser powder–based directed energy deposition process for additive manufacturing: a review, Int. J. Adv. Manuf. Technol. 107 (2020) 1959–1982, https://doi.org/10.1007/s00170-020-05027-0.

[19] A. Ebrahimi, M. Sattari, S.J.L. Bremer, M. Luckabauer, G.R.B.E. Römer, I. M. Richardson, C.R. Kleijn, M.J.M. Hermans, The influence of laser characteristics on internal flow behaviour in laser melting of metallic substrates, Mater. Des. 214 (2022) 110385, https://doi.org/10.1016/j.matdes.2022.110385.

[20] J. Wu, X. Zheng, Y. Zhang, S. Ren, C. Yin, Y. Cao, D. Zhang, Modeling of whole-phase heat transport in laser-based directed energy deposition with multichannel coaxial powder feeding, Addit. Manuf. 59 (2022) 103161, https://doi.org/10.1016/j.addma.2022.103161.

[21] B. Song, T. Yu, X. Jiang, W. Xi, X. Lin, Z. Ma, Z. Wang, Development of the molten pool and solidification characterization in single bead multilayer direct energy deposition, Addit. Manuf. 49 (2022) 102479, https://doi.org/10.1016/j.addma.2021.102479.

[22] Y. Huang, M.B. Khamesee, E. Toyserkani, A comprehensive analytical model for laser powder-fed additive manufacturing, Addit. Manuf. 12 (2016) 90–99, https://doi.org/10.1016/j.addma.2016.07.001.

[23] L. Chen, Y. Zhao, B. Song, T. Yu, Z. Liu, Modeling and simulation of 3D geometry prediction and dynamic solidification behavior of Fe-based coatings by laser cladding, Opt. Laser Technol. 139 (2021) 107009, https://doi.org/10.1016/j.optlastec.2021.107009.

[24] C. Vundru, R. Singh, W. Yan, S. Karagadde, A comprehensive analytical-computational model of laser directed energy deposition to predict deposition geometry and integrity for sustainable repair, Int. J. Mech. Sci. 211 (2021) 106790, https://doi.org/10.1016/j.ijmecsci.2021.106790.

[25] S.M. Thompson, L. Bian, N. Shamsaei, A. Yadollahi, An overview of direct laser deposition for additive manufacturing; Part I: transport phenomena, modeling and diagnostics, Addit. Manuf. 8 (2015) 36–62, https://doi.org/10.1016/j.addma.2015.07.001.

[26] D. De Lange, J. Hofman, J. Meijer, Influence of intensity distribution on the meltpool and clad shape for laser cladding, in: 2005: pp. 1–5.

[27] S.N. Grigoriev, A.V. Gusarov, A.S. Metel, T.V. Tarasova, M.A. Volosova, A. A. Okunkova, A.S. Gusev, Beam shaping in laser powder bed fusion: péclet number and dynamic simulation, Metals 12 (2022) 722, https://doi.org/10.3390/met12050722.

[28] M. Kubiak, W. Piekarska, S. Stano, Modelling of laser beam heat source based on experimental research of Yb:YAG laser power distribution, Int. J. Heat. Mass Transf. 83 (2015) 679–689, https://doi.org/10.1016/j.ijheatmasstransfer.2014.12.052.

[29] Y.M. Zhang, C.W.J. Lim, C. Tang, B. Li, Numerical investigation on heat transfer of melt pool and clad generation in directed energy deposition of stainless steel, Int. J. Therm. Sci. 165 (2021) 106954, https://doi.org/10.1016/j.ijthermalsci.2021.106954.

[30] Z. Gao, L. Wang, F. Lyu, Y. Zhang, T. Liu, X. Zhan, Temperature variation and mass transport simulations of invar alloy during continuous-wave laser melting deposition, Opt. Laser Technol. 152 (2022) 108163, https://doi.org/10.1016/j.optlastec.2022.108163.

[31] Oerlikon Metco, DSMTS-0078.5 – Austenitic Stainless Steel Powders, (2017).

[32] JMatPro the Materials Property Simulation Package, (2022). ⟨https://www.sentesoftware.co.uk/jmatpro⟩.

[33] J.J. Valencia, P.N. Quested, Thermophysical Properties, in: S. Viswanathan, D. Apelian, R.J. Donahue, B. DasGupta, M. Gywn, J.L. Jorstad, R.W. Monroe, M. Sahoo, T.E. Prucha, D. Twarog (Eds.), Casting, ASM International, 2008, pp. 468–481, https://doi.org/10.31399/asm.hb.v15.a0005240.

[34] FLOW-3D WELD, (2022).

[35] H.K. Versteeg, W. Malalasekera. An Introduction to Computational Fluid Dynamics: the Finite Volume Method, second ed, Pearson Education Ltd, Harlow, England; New York, 2007.

[36] A. Aggarwal, S. Patel, A.R. Vinod, A. Kumar, An integrated Eulerian-Lagrangian-Eulerian investigation of coaxial gas-powder flow and intensified particle-melt interaction in directed energy deposition process, Int. J. Therm. Sci. 166 (2021) 106963, https://doi.org/10.1016/j.ijthermalsci.2021.106963.

[37] V.R. Voller, C. Prakash, A fixed grid numerical modelling methodology for convection-diffusion mushy region phase-change problems, Int. J. Heat. Mass Transf. 30 (1987) 1709–1719, https://doi.org/10.1016/0017-9310(87)90317-6.

[38] L. Arnberg, L. Bäckerud, Solidification characteristics of aluminium alloys. 3: Dendrite coherency, Univ., Departm. of Structural Chemistry, Arrhenius Laboratory, Stockholm, 1996.

[39] P.S. Cook, A.B. Murphy, Simulation of melt pool behaviour during additive manufacturing: Underlying physics and progress, Addit. Manuf. 31 (2020) 100909, https://doi.org/10.1016/j.addma.2019.100909.

[40] M. Ma, Z. Wang, X. Zeng, A comparison on metallurgical behaviors of 316L stainless steel by selective laser melting and laser cladding deposition, Mater. Sci. Eng. A 685 (2017) 265–273, https://doi.org/10.1016/j.msea.2016.12.112.

[41] A. Ebrahimi, C.R. Kleijn, I.M. Richardson, Sensitivity of numerical predictions to the permeability coefficient in simulations of melting and solidification using the enthalpy-porosity method, Energies 12 (2019) 4360, https://doi.org/10.3390/en12224360.

[42] C.W. Hirt, B.D. Nichols, Volume of fluid (VOF) method for the dynamics of free boundaries, J. Comput. Phys. 39 (1981) 201–225, https://doi.org/10.1016/0021-9991(81)90145-5.

[43] J.U. Brackbill, D.B. Kothe, C. Zemach, A continuum method for modeling surface tension, J. Comput. Phys. 100 (1992) 335–354, https://doi.org/10.1016/0021-9991(92)90240-Y.

[44] K. Wark. Thermodynamics, fifth ed., McGraw-Hill, New York, 1988.

[45] Computational Techniques for Multiphase Flows, Elsevier, 2010. https://doi.org/10.1016/C2009-0-16604-7.

[46] R.F. Brooks, P.N. Quested, The surface tension of steels, J. Mater. Sci. 40 (2005) 2233–2238, https://doi.org/10.1007/s10853-005-1939-2.

[47] J. Xu, P. Zou, D. Kang, W. Wang, A. Wang, Research on the formation mechanism of the surface structure in transition regime of laser polishing 304 stainless steel,

Opt. Laser Technol. 149 (2022) 107906, https://doi.org/10.1016/j.optlastec.2022.107906.
[48] Z.S. Saldi, A. Kidess, S. Kenjereš, C. Zhao, I.M. Richardson, C.R. Kleijn, Effect of enhanced heat and mass transport and flow reversal during cool down on weld pool shapes in laser spot welding of steel, Int. J. Heat. Mass Transf. 66 (2013) 879–888, https://doi.org/10.1016/j.ijheatmasstransfer.2013.07.085.
[49] Y. Wang, Q. Shi, H.L. Tsai, Modeling of the effects of surface-active elements on flow patterns and weld penetration, Metall. Mater. Trans. B 32 (2001) 145–161, https://doi.org/10.1007/s11663-001-0017-7.
[50] P. Sahoo, T. Debroy, M.J. McNallan, Surface tension of binary metal—surface active solute systems under conditions relevant to welding metallurgy, Metall. Trans. B 19 (1988) 483–491, https://doi.org/10.1007/BF02657748.
[51] Y. Wang, M. Zhou, X. Pang, X. Chen, Z. Wang, A. Volinsky, H. Tang, Thermodynamic analysis of Ti3O5nanoparticles formed in melt and their effects on ferritic steel microstructure, Materials 11 (2018) 1343, https://doi.org/10.3390/ma11081343.
[52] M.J. McNallan, T. Debroy, Effect of temperature and composition on surface tension in Fe-Ni-Cr alloys containing sulfur, Metall. Trans. B 22 (1991) 557–560, https://doi.org/10.1007/BF02654294.
[53] E. Ichise, A. Moro-Oka, Interaction parameter in liquid iron alloys, Trans. Iron Steel Inst. Jpn. 28 (1988) 153–163, https://doi.org/10.2355/isijinternational1966.28.153.
[54] M. Bayat, V.K. Nadimpalli, F.G. Biondani, S. Jafarzadeh, J. Thorborg, N.S. Tiedje, G. Bissacco, D.B. Pedersen, J.H. Hattel, On the role of the powder stream on the heat and fluid flow conditions during Directed Energy Deposition of maraging steel—multiphysics modeling and experimental validation, Addit. Manuf. 43 (2021) 102021, https://doi.org/10.1016/j.addma.2021.102021.
[55] J.-H. Cho, S.-J. Na, Implementation of real-time multiple reflection and Fresnel absorption of laser beam in keyhole, J. Phys. Appl. Phys. 39 (2006) 5372–5378, https://doi.org/10.1088/0022-3727/39/24/039.
[56] P.A. Cundall, O.D.L. Strack, A discrete numerical model for granular assemblies, Géotechnique 29 (1979) 47–65, https://doi.org/10.1680/geot.1979.29.1.47.
[57] T.L. Bergman, F.P. Incropera. Fundamentals of heat and mass transfer, seventh ed., Wiley, Hoboken, NJ, 2011 (eds.).
[58] S. Yu, J. Wang, C. Chen, R. Wang, S. Xu, J. Zhao, Z. Ren, Thermo-fluid dynamics and morphology evolution of nickel-based superalloy in a multilayer laser directed energy deposition process, J. Mater. Res. Technol. 28 (2024) 1276–1293, https://doi.org/10.1016/j.jmrt.2023.12.047.
[59] A.J. Pinkerton, L. Li, Modelling powder concentration distribution from a coaxial deposition nozzle for laser-based rapid tooling, J. Manuf. Sci. Eng. 126 (2004) 33–41, https://doi.org/10.1115/1.1643748.
[60] J. Ibarra-Medina, A.J. Pinkerton, Numerical investigation of powder heating in coaxial laser metal deposition, Surf. Eng. 27 (2011) 754–761, https://doi.org/10.1179/1743294411Y.0000000017.
[61] Y. Fu, A. Loredo, B. Martin, A.B. Vannes, A theoretical model for laser and powder particles interaction during laser cladding, J. Mater. Process. Technol. 128 (2002) 106–112, https://doi.org/10.1016/S0924-0136(02)00433-8.
[62] Y.-L. Huang, J. Liu, N.-H. Ma, J.-G. Li, Three-dimensional analytical model on laser-powder interaction during laser cladding, J. Laser Appl. 18 (2006) 42–46, https://doi.org/10.2351/1.2164476.
[63] F. Brückner, D. Lepski, E. Beyer, Modeling the influence of process parameters and additional heat sources on residual stresses in laser cladding, J. Therm. Spray. Technol. 16 (2007) 355–373, https://doi.org/10.1007/s11666-007-9026-7.
[64] H. Liu, Y. Zhou, An interaction model for laser and powder in wide-beam laser cladding, Int. J. Adv. Manuf. Technol. 112 (2021) 15–23, https://doi.org/10.1007/s00170-020-06330-6.
[65] A.J. Pinkerton, R. Moat, K. Shah, L. Li, M. Preuss, P.J. WithersA verified model of laser direct metal deposition using an analytical enthalpy balance method Orlando, Florida, USA , Laser Institute of America , Int. Congr. Appl. Lasers Electro-Opt. , 2007, , 1806, 10.2351/1.5061038.
[66] I. Tabernero, A. Lamikiz, S. Martínez, E. Ukar, L.N. López De Lacalle, Modelling of energy attenuation due to powder flow-laser beam interaction during laser cladding process, J. Mater. Process. Technol. 212 (2012) 516–522, https://doi.org/10.1016/j.jmatprotec.2011.10.019.
[67] J. Wang, Z. Zhang, F. Han, S. Chen, W. Ying, Modeling of laser power attenuation by powder particles for laser solid forming, Procedia CIRP 95 (2020) 42–47, https://doi.org/10.1016/j.procir.2020.02.286.
[68] N. Sobhanieh, J. Akbari, M. Moradi, A new method for calculating laser intensity distribution on workpiece surface in laser-directed energy deposition process by considering powder stream distribution and laser attenuation, Int. J. Adv. Manuf. Technol. 121 (2022) 337–348, https://doi.org/10.1007/s00170-022-09301-1.
[69] W. Jiazhu, T. Liu, H. Chen, F. Li, H. Wei, Y. Zhang, Simulation of laser attenuation and heat transport during direct metal deposition considering beam profile, J. Mater. Process. Technol. 270 (2019) 92–105, https://doi.org/10.1016/j.jmatprotec.2019.02.021.
[70] J. Ibarra-Medina, A.J. Pinkerton, A CFD model of the laser, coaxial powder stream and substrate interaction in laser cladding, Phys. Procedia 5 (2010) 337–346, https://doi.org/10.1016/j.phpro.2010.08.060.
[71] W. Devesse, D. De Baere, P. Guillaume, Modeling of laser beam and powder flow interaction in laser cladding using ray-tracing, J. Laser Appl. 27 (2015) S29208, https://doi.org/10.2351/1.4906394.
[72] X. Guan, Y.F. Zhao, Numerical modeling of coaxial powder stream in laser-powder-based directed energy deposition process, Addit. Manuf. 34 (2020) 101226, https://doi.org/10.1016/j.addma.2020.101226.
[73] V.G. Gusev, A.V. Sobolkov, A.V. Aborkin, Determination of the coefficient of restitution upon contact of a steel ball with aluminum and steel surfaces, J. Phys. Conf. Ser. 2131 (2021) 032087, https://doi.org/10.1088/1742-6596/2131/3/032087.
[74] S.M.A. Noori Rahim Abadi, Y. Mi, F. Sikström, I. Choquet, Influence of Laser Beam Shaping on Melt Pool Thermocapillary Flow, in: 2020. ⟨https://doi.org/10.11159/htff20.125⟩.
[75] The MathWorks Inc., MATLAB, (2023). ⟨https://www.mathworks.com⟩.
[76] FLOW-3D, (2022). ⟨https://www.flow3d.com/products/flow-3d/flow-3d-2022r1/⟩.
[77] M.-J. Li, J. Chen, Y. Lian, F. Xiong, D. Fang, An efficient and high-fidelity local multi-mesh finite volume method for heat transfer and fluid flow problems in metal additive manufacturing, Comput. Methods Appl. Mech. Eng. 404 (2023) 115828, https://doi.org/10.1016/j.cma.2022.115828.
[78] Y. Saad, Iterative methods for sparse linear systems, PWS Pub. Co, Boston, 1996.
[79] M.R. Hestenes, E. Stiefel, et al., Methods of conjugate gradients for solving linear systems, J. Res. Natl. Bur. Stand 49 (1952) 409–436.
[80] S. Wang, L. Zhu, J.Y.H. Fuh, H. Zhang, W. Yan, Multi-physics modeling and Gaussian process regression analysis of cladding track geometry for direct energy deposition, Opt. Lasers Eng. 127 (2020) 105950, https://doi.org/10.1016/j.optlaseng.2019.105950.
[81] K.M. Nagaraja, W. Li, D. Qian, V. Vasudevan, Y. Pyun, H. Lu, Multiphysics modeling of in situ integration of directed energy deposition with ultrasonic nanocrystal surface modification, Int. J. Adv. Manuf. Technol. 120 (2022) 5299–5310, https://doi.org/10.1007/s00170-022-09082-7.
[82] X. Kaikai, G. Yadong, Z. Qiang, Numerical simulation of dynamic analysis of molten pool in the process of direct energy deposition, Int. J. Adv. Manuf. Technol. 124 (2023) 2451–2461, https://doi.org/10.1007/s00170-022-10271-7.
[83] T. Mukherjee, V. Manvatkar, A. De, T. DebRoy, Dimensionless numbers in additive manufacturing, J. Appl. Phys. 121 (2017) 064904, https://doi.org/10.1063/1.4976006.
[84] G. Li, Z. Wang, L. Yao, J. Ding, J. Gao, Component mixing in laser cladding processes: from single-track to single-layer multi-track and multi-layer multi-track, Surf. Coat. Technol. 455 (2023) 129233, https://doi.org/10.1016/j.surfcoat.2023.129233.
[85] D. Wu, A. Van Nguyen, S. Tashiro, X. Hua, M. Tanaka, Elucidation of the weld pool convection and keyhole formation mechanism in the keyhole plasma arc welding, Int. J. Heat. Mass Transf. 131 (2019) 920–931, https://doi.org/10.1016/j.ijheatmasstransfer.2018.11.108.
[86] A.H. Faraji, C. Maletta, G. Barbieri, F. Cognini, L. Bruno, Numerical modeling of fluid flow, heat, and mass transfer for similar and dissimilar laser welding of Ti-6Al-4V and Inconel 718, Int. J. Adv. Manuf. Technol. 114 (2021) 899–914, https://doi.org/10.1007/s00170-021-06868-z.
[87] A.K. Unni, V. Muthukumaran, Modeling of heat transfer, fluid flow, and weld pool dynamics during keyhole laser welding of 316 LN stainless steel using hybrid conical-cylindrical heat source, Int. J. Adv. Manuf. Technol. 122 (2022) 3623–3645, https://doi.org/10.1007/s00170-022-09946-y.
[88] Y. Lee, D.F. Farson, Simulation of transport phenomena and melt pool shape for multiple layer additive manufacturing, J. Laser Appl. 28 (2016) 012006, https://doi.org/10.2351/1.4935711.
[89] F.Q. Liu, L. Wei, S.Q. Shi, H.L. Wei, On the varieties of build features during multi-layer laser directed energy deposition, Addit. Manuf. 36 (2020) 101491, https://doi.org/10.1016/j.addma.2020.101491.
[90] A. Ebrahimi, M.J.M. Hermans, Laser butt welding of thin stainless steel 316L sheets in asymmetric configurations: A numerical study, J. Adv. Join. Process. 8 (2023) 100154, https://doi.org/10.1016/j.jajp.2023.100154.